Published in final edited form as:
*Nat Metab*. 2021 February 01; 3(2): 211–227. doi:10.1038/s42255-021-00341-7.

# Diet-dependent regulation of TGFβ impairs reparative innate immune responses after demyelination

**Mar Bosch-Queralt**[1,2], **Ludovico Cantuti-Castelvetri**[1,2], **Alkmini Damkou**[1,2], **Martina Schifferer**[2,3], **Kai Schlepckow**[2], **Ioannis Alexopoulos**[1,2], **Dieter Lütjohann**[4], **Christian Klose**[5], **Lenka Vaculčiaková**[6], **Takahiro Masuda**[7], **Marco Prinz**[7,8,9], **Kathryn M. Monroe**[10], **Gilbert Di Paolo**[10], **Joseph W. Lewcock**[10], **Christian Haass**[2,3,11], **Mikael Simons**✉[,1,2,3]

[1]Institute of Neuronal Cell Biology, Technical University Munich, Munich, Germany

[2]German Center for Neurodegenerative Diseases (DZNE), Munich, Germany

[3]Munich Cluster of Systems Neurology (SyNergy), Munich, Germany

[4]institute for of Clinical Chemistry and Clinical Pharmacology, University of Hospital Bonn, Bonn, Germany

[5]Lipotype, Dresden, Germany

[6]Department of Neurophysics, Max Planck Institute for Human Cognitive and Brain Sciences, Leipzig, Germany

[7]Institute of Neuropathology, Faculty of Medicine, University of Freiburg, Freiburg, Germany

[8]Signalling Research Centres BIOSS and CIBSS, University of Freiburg, Freiburg, Germany

[9]Center for Basics in NeuroModulation (NeuroModulBasics), Faculty of Medicine, University of Freiburg, Freiburg, Germany

[10]Denali Therapeutics Inc., South San Francisco, California, USA

[11]Chair of Metabolic Biochemistry, Biomedical Center (BMC), Faculty of Medicine, Ludwig-Maximilians-Universität München, Munich, Germany

✉**Correspondence and requests for materials** should be addressed to M.S. mikael.simons@dzne.de.

**Reporting Summary**. Further information on research design is available in the Nature Research Reporting Summary linked to this article.

**Author contributions**

M.B.-Q. and M.S. conceived the project and designed experiments. M.B.-Q., L.C.-C., A.D., M. Schifferer., D.L., C.K. carried out experiments, K.S., L.V., I.A., T.M., M.P., L.M., G.D.P., K.M.M,, J.W.L, C.H developed and provided tools, M.B-Q., L.C-C., A.D., M. Simons, D.L., C.K. analysed the data or supervised data acquisition. M.B-Q. visualized the data, M.B-Q. and M.S wrote the manuscript, M.S supervised the project.

**Competing interests**

G.D.P., K.M.M and J.W.L are paid employees and shareholders of Denali Therapeutics Inc. C.K. is an employee of Lipotype.

**Extended data** is available for this paper at https://doi.org/10.1038/s42255-021-00341-7.

**Peer review information** *Nature Metabolism* thanks Michela Matteoli and the other, anonymous, reviewer(s) for their contribution to the peer review of this work. Primary Handling Editors: George Caputa; Elena Bellafante.

**Reprints and permissions information** is available at www.nature.com/reprints.

**Publisher's note** Springer Nature remains neutral with regard to jurisdictional claims in published maps and institutional affiliations.


Europe PMC Funders Author Manuscripts

Europe PMC Funders Author Manuscripts


## Abstract

Proregenerative responses are required for the restoration of nervous-system functionality in demyelinating diseases such as multiple sclerosis (MS). Yet, the limiting factors responsible for poor CNS repair are only partially understood. Here, we test the impact of a Western diet (WD) on phagocyte function in a mouse model of demyelinating injury that requires microglial innate immune function for a regenerative response to occur. We find that WD feeding triggers an ageing-related, dysfunctional metabolic response that is associated with impaired myelin-debris clearance in microglia, thereby impairing lesion recovery after demyelination. Mechanistically, we detect enhanced transforming growth factor beta (TGFβ) signalling, which suppresses the activation of the liver X receptor (LXR)-regulated genes involved in cholesterol efflux, thereby inhibiting phagocytic clearance of myelin and cholesterol. Blocking TGFβ or promoting triggering receptor expressed on myeloid cells 2 (TREM2) activity restores microglia responsiveness and myelin-debris clearance after demyelinating injury. Thus, we have identified a druggable microglial immune checkpoint mechanism regulating the microglial response to injury that promotes remyelination.


The transition of large parts of the world to a WD high in calories, fat and sugar represents one of the most profound environmental changes that has occurred over the past generations. One feature associated with WD consumption is chronic systemic inflammation characterized by proinflammatory processes involving peripheral cells of the innate immune system[13]. While obesity-induced inflammation in peripheral tissues is extensively studied, the mechanisms of WD-induced effects on microglia-mediated innate immunity in the central nervous system (CNS) are less clear. To examine this question, we focused on a model of demyelinating injury that requires innate immune function for a regenerative response to occur. Following demyelination, microglia/macrophages proliferate and enter demyelinating lesions, where their prime task is to phagocytose, metabolize and clear damaged myelin[4–9]. Myelin intake poses a challenge to phagocytes, as myelin is composed of tightly packed membrane stacks that are difficult to degrade[10]. In addition, myelin is rich in cholesterol, which cannot be broken down, and therefore needs to be transferred from the phagocytes to the extracellular space onto lipoprotein particles. Only when this clearance process is terminated does inflammation resolve and remyelination follow[11,12]. However, in demyelinating diseases such as multiple sclerosis (MS), the capacity for remyelination is limited and varies between people[13–17]. An improved understanding of disease mechanisms will enable the development of proregenerative therapies[5,18,19]. One of the primary and best-understood reasons for the decline in remyelination efficiency is ageing. With ageing, the activation, recruitment and differentiation of oligodendrocyte progenitors (OPCs) are altered, and the efficiency of microglia/macrophages to clear myelin debris also declines[8,20–24]. Apart from age, other factors that contribute to poor remyelination are unclear. Previous studies indicate that obesity may increase the risk of developing MS and accelerate the progression of MS towards increasing disability[25,26]. As WD significantly alters macrophage metabolism in peripheral organs, we hypothesized that WD might influence the brain microenvironment, microglia metabolic functions and, ultimately, remyelination.

## Results

### Western diet impairs lesion recovery after demyelinating injury

To analyse the effects of diets on the regenerative response after demyelinating injury in mice, we fed 6-week-old C57BL/6J mice either a WD or control diet (CD) for 8 to 10 weeks[27] (Fig. 1a). The WD had a high fat content, in which 42% of the metabolizable energy came from fat, while the ratio was 13% in the CD (Fig. 1b,c). WD-fed mice rapidly increased their weight to 34.76 g, on average, after 10 weeks of feeding, while mice on CD weighed 27.74 g on average (Fig. 1d,e). To determine whether WD-induced plasma lipid alterations influence brain lipid composition, we performed quantitative shotgun lipidomics on plasma and brain grey and white matter from transcardially perfused WD- and CD-fed mice. As expected, the plasma lipid profile was completely altered by WD consumption (Extended Data Fig. 1a–e). Lipids from WD mouse plasma were characterized by increased saturation (Extended Data Fig. 1c) and a shorter chain length (Extended Data Fig. 1e), which correlates with the properties of the diet lipid content. Principal component analysis (PCA) also showed segregation of the brain lipidome samples from WD- and CD-fed mice (Extended Data Fig. 2a). Brains of WD-fed mice were characterized by a higher percentage of saturated lipids with shorter acyl length both in the grey (Extended Data Fig. 2h,i) and the white matter (Extended Data Fig. 2f,g), which correlated to the changes observed in the plasma. Blood-brain barrier (BBB) permeability was not affected by WD feeding, as evaluated by the injection of fluorescently labelled Evans blue (Extended Data Fig. 3d,h). Together, these findings indicate that WD feeding induced alterations in the plasma lipid profile that extend into the brain. Next, we performed immunohistochemistry to determine whether WD feeding induces an increase in lipid storage, evaluated by the formation of lipid droplets within cells. We found an increased number of lipid droplets in the lateral ventricle wall, in contact with the corpus callosum (Extended Data Fig. 2l–n). In addition, we detected an increased percentage of microglia and astrocytes containing $PLIN2^+$ lipid droplets in the corpus callosum of WD-fed mice (Extended Data Fig. 2o–q,u,t). We determined the number of microglia in the corpus callosum and found that the $IBA1^+$ cell density and signal intensity increased significantly in the corpus callosum in WD-fed mice compared with that in CD-fed mice (Extended Data Fig. 2r,s), whereas $GFAP^+$ immunoreactivity remained unchanged (Extended Data Fig. 2v,w). We further immunostained microglia using three microglia activation markers, CLEC7A, AXL and MAC2, and detected more $CLEC7A^+IBA1^+$ cells in the corpus callosum in WD-fed mice than in CD-fed mice (Extended Data Fig. 3a,e), while the two other activation markers did not show significant differences (Extended Data Fig. 3b,c,f,g). Thus, microglia appear to weakly respond to changes that occur in the white matter during WD feeding.

To determine the effects of WD on CNS lesion recovery, we employed a toxin-induced model in which a single injection of lyso-phosphatidylcholine (or lysolecithin, LLC) is injected to the corpus callosum or the spinal cord to induce a focal demyelinating lesion in the white matter. Demyelination is complete within 4 days and is followed by a repair process that is at its maximum between 14 to 21 days post injection (dpi) and requires rapid clearance of damaged myelin by phagocytes[28]. In this model, microglia represent the major phagocyte population, as only relatively few monocyte-derived macrophages enter lesions

from the periphery[29,30]. We used fluorescent myelin staining (FluoroMyelin) to determine lesion sizes and antibodies against IBA1 to quantify the number of phagocytes in lesioned animals. At 4 dpi, demyelinating lesions were of similar size in WD- and CD-fed mice, and comparable volumes of the lesions were occupied by IBA1$^+$ phagocytes (Fig. 1f-h), showing that lesion formation was unaltered. However, when lesion sizes were analysed at 14 dpi, we observed that lesions remained large in WD-fed mice, pointing to impaired lesion recovery (Fig. 1f,g,i). In addition, quantification of the volume occupied by IBA1$^+$ cells revealed a sustained immune response (Fig. 1f,g,i). Furthermore, quantification of oligodendrocytes using antibodies against anti-adenomatous polyposis coli (APC), clone CC1, revealed a lower number mature CC1$^+$ oligodendrocytes in lesions of WD-fed mice at 14 dpi (Fig. 1j,k). Thus, WD feeding results in sustained inflammation and poor lesion recovery after demyelinating injury in mice.

To assess whether the diet per se or the conditions induced by it were responsible for poor lesion recovery, we used leptin-deficient mice (lep$^{ob/ob}$, *ob/ob*), fed a normal control diet, as a genetically induced model of obesity. Leptin is a hormone secreted by adipocytes that plays a critical role in the control of feeding. Mice lacking circulating leptin are hyperphagic and obese[31]. We induced demyelinating lesions in 3-month-old *ob/ob* mice and observed, as in WD-fed mice, that lesion size did not differ initially, at 4 dpi, with that in controls (Fig. 1l-n). However, when lesions were analysed at 14 dpi, we detected larger lesions and more IBA1$^+$ cells (Fig. 1l,m,o) in lep$^{ob/ob}$ mice than in control mice. Thus, both diet and genetically induced obesity results in sustained inflammation and poor lesion recovery after demyelinating injury in mice.

## Correcting metabolic alterations improves lesion repair after demyelination

Consumption of WD induces a large range of metabolic alterations including dyslipidaemia (Extended Data Fig. 1a–e) and glucose intolerance (Extended Data Fig. 1f). Next, we determined whether pharmacological interventions of these conditions were able to improve recovery from demyelinating injury. For this, we applied fenofibrate (FF) and rosiglitazone (RG), peroxisome proliferator-activated receptor (PPAR) agonists, which are used to treat dyslipidaemia or diabetes[32]. WD-fed lesioned animals were treated with FF, RG or control, and serial sections were generated to determine lesion sizes. Treatment with both drugs led to improved lesion regeneration as assessed by FluoroMyelin staining (Fig. 2a-c). Immunohistochemistry revealed a reduction in the volume occupied by IBA1$^+$ cells (Fig. 2a-c). To determine whether stimulation of these same pathways was also beneficial for recovery in ageing, 12-month-old mice were treated from the day of LLC injection with FF, RG or vehicle control, and lesion sizes were determined. Neither FF nor RG showed beneficial effects in promoting lesion recovery of 12-month-old mice (Fig. 2d). Thus, stimulating PPARs improves lesion recovery induced by WD feeding, but does not represent a general strategy for promoting lesion recovery after demyelinating injury.

## WD feeding impairs myelin-debris clearance in demyelinating lesions

Phagocytes play an important role in clearance of myelin lipid debris and in promoting a regenerative response after demyelination[8,21,33–35]. Thus, we determined whether WD feeding impairs myelin-debris clearance and lipid processing by phagocytes in lesions at 14

dpi. First, we quantified the number of IBA1$^+$ phagocytes containing myelin debris, labelled using FluoroMyelin and antibodies against proteolipid protein (PLP). Indeed, lesions of WD-fed mice contained higher numbers of myelin-laden phagocytes than did those in CD-fed mice (Fig. 3a-c). By combining laser reflection and fluorescence confocal microscopy (reflection microscopy) to image crystals, we detected higher numbers of crystal-loaded IBA1$^+$ phagocytes in the lesions of WD-fed mice (Fig. 3c,d). Light microscopy of resin-embedded semithin sections revealed increased amounts of foam cells containing lipid droplets (Fig. 3e,f). Using transmission electron microscopy (Fig. 3g) and confocal microscopy (Extended Data Fig. 4h), we localized crystal deposition to both lysosomes and lipid droplets. Microglia in 14 dpi lesions of WD-fed mice displayed more LAMP1 labeling (Fig. 3h), which colocalized with both myelin debris and crystals (Fig. 3j). We found that both FF and RG treatment decreased the number of myelin-loaded phagocytes (Extended Data Fig. 4e,g), while only FF decreased the number of crystal-loaded phagocytes in the lesions (Extended Data Fig. 4f,g). No differences in crystals were observed upon RG treatment, possibly due to the function of RG in promoting lipid-droplet formation and storage. When lesions were evaluated at 4 dpi, we did not detect any differences in the number of IBA1$^+$ phagocytes containing myelin debris (Fig. 3i,l) or with a foam-cell morphology (Fig. 3k,m) between WD- and CD-fed mice. We also observed no differences in IBA1$^+$ cell density at 4 and 7dpi (Extended Data Fig. 4a,b), providing evidence that differences occur during lesion recovery. Thus we observed typical hallmarks of cholesterol overloading of phagocytes after inducing demyelinating injury in WD-fed mice, pointing to defective lipid processing.

## The LXR pathway is poorly upregulated in WD-fed mice

After phagocytosis, myelin-derived cholesterol needs to be transferred from the phagocytes back to the extracellular space by employing the transporters ATP-binding cassette A1 and G1 (ABCA1 and ABCG1) and APOE lipoprotein particles as acceptors[36]. This reverse cholesterol pathway is under the control of liver X receptor (LXR), which enhances the expression of *Apoe, Abcal* and *Abcgl* transcripts. To evaluate whether this pathway was poorly activated in WD-fed mice, we isolated RNA from 2 and 7 dpi lesions of WD- and CD-fed mice and determined the expression of LXR target genes implicated in reverse cholesterol transport by quantitative reverse transcription PCR (RT–qPCR), and found that their induction was impaired in lesions of WD-fed mice. There was a lower elevation of *Apoe* ($P$=0.02) and *Abcal* ($P$ = 0.01), and tendentially of *Abcgl* ($P$=0.06), transcripts in lesions of WD-fed mice than in those of CD-fed mice (Fig. 4a). The reduced induction of APOE in lesions of WD-compared with in CD-fed mice was confirmed at the protein level (Extended Data Fig. 4c,d). Furthermore, by using RNA in situ labelling to evaluate the expression of *Abcal* and *Abcgl* by phagocytes in 14 dpi lesions, we observed that the lower expression of *Abcal* ($P$ = 0.03) persisted in WD-fed mice (Fig. 4b). Thus, one possible explanation for poor lesion recovery in WD-fed mice could be the failure to activate the LXR-dependent cholesterol efflux pathway, known to be required in myeloid cells after myelin phagocytosis[21,37]. To assess whether the activation of lipid-processing pathways could promote recovery of demyelinated lesions, we conducted a pharmacological approach by targeting LXR to induce transcriptional changes for reverse cholesterol transport. We treated WD-fed mice with the LXR agonist GW3965 (GW) and found that treatment with

GW led to markedly improved lesion regeneration as assessed by FluoroMyelin staining (Fig. 4c,g). Immunohistochemistry revealed a reduction in the volume occupied by IBA1$^+$ cells (Fig. 4d,g). In addition, the number of IBA1$^+$ cells containing myelin debris and the amount of crystals, as assessed by reflection microscopy, was reduced (Fig. 4e,f,h). The beneficial effect of GW suggests that genes induced by the transcription factor LXR could be critical for lesion recovery after WD feeding.

## TGFβ signalling increases in the brain after WD feeding

To understand why the cholesterol efflux pathway was not appropriately activated in lesions of WD-fed mice, we first quantified des-mosterol and oxysterols (hydroxylated cholesterol metabolites), 24S-hydroxycholesterol and 27-hydroxycholesterol, the endogenous LXR ligands that control the expression of genes involved in cholesterol efflux in cholesterol-loaded cells[38,39] (Extended Data Fig. 4i). Using gas chromatography-mass spectrometry (GC/MS) we determined the levels of desmosterol, 24S-hydroxycholesterol and 27-hydroxycholesterol in 4 and 7 dpi lesions of WD- and CD-fed mice, but did not detect any differences that could explain the poor induction of the LXR pathway observed in WD mice (Extended Data Fig. 4j-l).

Another possible explanation for the reduced induction of cholesterol efflux genes in lesions of WD-fed mice is impaired activation of phagocytes in early time points after demyelination[5]. To examine microglia and macrophage reactivity, we induced lesions by LLC injection in the corpus callosum of WD- and CD-fed mice and examined phagocyte activation at 4 dpi by immunohistochemistry, using antibodies against MHCII and MAC2. Surprisingly, we detected lower percentages of MHCII$^+$IBA1$^+$ ($P = 0.01$) (Fig. 5a,b and Extended Data Fig. 5a) and MAC2$^+$IBA1$^+$ ($P = 0.02$) (Fig. 5c,d and Extended Data Fig. 5b) cells in lesions of WD mice. Since these results suggested that WD could be locking microglia in an unresponsive state, we examined factors controlling microglia responsiveness. Previous work has provided evidence that TGFβ levels increase in obesity in adipose tissue, plasma and brain[40,41]. TGFβ is known to promote the homeostatic transcriptional programme of microglia and to block the transition into a disease-associated microglia state[42]. Therefore, we hypothesized that WD may induce TGFβ expression in the brain, thereby suppressing microglia responsiveness after demyelinating lesion induction. Using RT– qPCR, we first assessed *Tgfbl* and *Tgfb2* transcript levels in the unlesioned brain and found increased levels in WD-fed mice compared with those in controls (Extended Data Fig. 5d). We confirmed these findings using RNA in situ labelling of *Tgfbl* and *Tgfb2* in the corpus callosum, where we detected increased expression of *Tgfbl* (Extended Data Fig. 5c,e), in particular in astrocytes (Extended Data Fig. 5f-h). Next, we isolated RNA from lesioned CD- and WD-fed mice at 2 dpi and evaluated the expression of *Tgfbl* and *Tgfb2*. Surprisingly, the overexpression of TGFβ ligands persisted at this early time point after demyelination (Fig. 5e). We observed that approximately 90% of *Tgfbl* and 70% of *Tgfb2* of RNA in situ labelling signal were derived from microglia and astrocytes (Extended Data Fig. 6a-c). Next, we quantified the amount of each TGFβ ligand in microglia or astrocytes in 2 dpi lesions of CD- and WD-fed mice and detected significantly more *Tgfbl* and *Tgfb2* RNA in situ signal in astrocytes (Fig. 5f-h). In addition, there was an increased number of GFAP$^+$ astrocytes in lesions of WD-fed mice at 4 dpi (Fig. 5j,p), but not at 14 dpi (Fig. 5k),

indicating that GFAP$^+$ astrocytes could be involved in generating excessive amounts of TGFβ in lesions at an early time point after demyelination. Enzyme-linked immunosorbent assay (ELISA) of TGFβ1 levels in lesions from CD- and WD-fed mice did not reveal significant differences (Extended Data Fig. 5i). To determine whether TGFβ signalling increased in phagocytes of lesioned WD-fed mice, we stained demyelinated lesions at 4 dpi for phosphorylated SMAD2 (pSMAD2). SMAD2 is a signalling molecule downstream of the TGFβ receptor, and upon TGFβ binding on the receptor, SMAD2 gets phosphorylated (pSMAD2) and translocated into the nucleus[43]. Despite a similar number of cells in the lesions, there was a higher percentage of area covered by the pSMAD2 staining (Fig. 5l,m,q). Furthermore, we found a higher percentage of pSMAD2$^+$ signal that colocalized with microglia within the demyelinated lesions (Fig. 5n,r) and in the unlesioned corpus callosum (Extended Data Fig. 5j,k) in WD-fed mice. To confirm these findings, we stained for pSMAD3, another signalling molecule downstream of the TGFβ receptor, and found increased pSMAD3 signal within IBA1$^+$ phagocytes in the lesions of WD-fed mice (Fig. 5o,s). Because consumption of WD induces dys-lipidaemia and hyperglycaemia, we incubated primary microglia and astrocytes with glucose and lipids in vitro to determine whether this was sufficient to trigger increased TGFβ production. Elevated glucose levels induced *Tgfb2* expression by microglia (Extended Data Fig. 6d), while treatment with a mixture of lipids (including saturated fatty acids and sterols) increased *Tgfb2* expression in both microglia and astrocytes (Extended Data Fig. 6e,f). Together, these findings provide evidence that WD feeding increases TGFβ signalling in the brain, which persists at early time points after demyelination, raising the question of whether this is the underlying cause for impaired phagocyte activation and lipid processing.

## TGFβ blocks LXR target gene induction after myelin uptake

To determine whether the increased TGFβ signalling suppresses the induction of cholesterol efflux genes in phagocytes, we examined the pathway in vitro using cultured primary microglia (Fig. 6a). First, we used RT-qPCR, and confirmed previous results showing that myelin debris internalization induces the expression of genes involved in cholesterol efflux[40]. We found that expression of *Abcal* and *Abcg1* transcripts increased 4 and 24 hours after myelin phagocytosis (Fig. 6c,d, grey dots). Notably, when microglia were treated with TGFβ, we found that the induction of *Abca1* and *Abcg1* transcripts was repressed (Fig. 6c,d, green dots). We confirmed these results using bone-marrow-derived macrophages (BMDMs), in which treatment with TGFβ prevented the induction of *Abca1* and *Abcg1* expression 4hours after myelin intake (Fig. 6e). We validated that TGFβ did not change *Abca1* and *Abcg1* levels in cells in the absence of myelin-debris treatment (Fig. 6f). Next, we tested whether TGFβ affects myelin phagocytosis, but did not observe any differences in the extent of myelin debris internalization (Fig. 6b). Thus, our data provide evidence that TGFβ signalling suppresses genes required for cholesterol efflux after myelin debris uptake in microglia and macrophages.

## Blocking TGFβ signalling in WD-fed mice promotes lesion recovery

To determine whether WD-induced excess TGFβ signalling was responsible for the insufficient activation of the LXR pathway and poor lesion recovery in WD-fed mice, a conditional microglia/macrophage-specific mutant mouse line for *Tgfbr2* was generated by

crossing *Cx3cr1*$^{CreERT2}$ mice with mice carrying floxed alleles of *Tgfbr2* to obtain *Cx3cr1*$^{CreERT}$:*Tgfbr2*$^{fl/fl}$ (Tgfbr2 KO) mice[44] (Fig. 7j). First, we confirmed the deletion of *Tgfbr2* at 2 weeks after tamoxifen treatment by analysing the expression of the transcript by RT-qPCR (Extended Data Fig. 7a) and RNA in situ hybridization (Extended Data Fig. 7b,c). We validated these results at the protein level by examining the TGFβR2 levels in microglia isolated from Tgfbr2 KO and control mice (Extended Data Fig. 7d,e). Next, we isolated RNA from demyelinated lesions at 2 and 7 dpi and analysed the expression of *Apoe, Abca1* and *Abcg1* transcripts in Tgfbr2 KO and control mice and found that their induction was enhanced in lesions of Tgfbr2 KO. There was a significantly higher increase in *Apoe* and *Abca1* transcripts, while *Abcg1* mRNA levels were unchanged in lesions of Tgfbr2 KO as compared with control. Next, we induced demyelinating lesions and analysed mice at 4 and 14 dpi to determine possible differences in lesion recovery. We observed no differences in the extent of demyelination or the amount of IBA1$^{+}$ cells at 4 dpi (Extended Data Fig. 7f,g). However, when lesions were analysed at 14 dpi, we detected enhanced lesion recovery in Tgfbr2 KO mice as compared with that in control mice (Fig. 7b,e). Immunohistochemistry revealed a reduction of IBA1$^{+}$ cells (Fig. 7d,e), and colabelling with FluoroMyelin showed less accumulation of myelin debris within lysosomes of phagocytes (Fig. 7g,i). Using reflection microscopy, we found decreased crystal deposition in lesions of Tgfbr2 KO mice (Fig. 7h,i). Because WD feeding induces TGFβ signalling, we evaluated whether enhanced recovery was specific to WD-fed mice or was also observed in CD-fed mice. Lesion recovery did not improve in Tgfbr2 KO mice, which were fed a CD (Fig. 7c,f and Extended Data Fig. 7h,i), supporting our conclusion that WD induces TGFβ signalling in microglia and macrophages that impedes the regenerative response.

Next, we asked whether we could confirm our findings by using a pharmacological approach and tested the effect of galunisertib, a TGFβRI blocker[45], in WD-fed mice (Fig. 7j). Lesioned WD-fed mice were treated for 14 days with galunisertib or vehicle control, and serial sections were generated to determine lesion sizes. Treatment with galunisertib led to improved lesion regeneration in WD-fed mice (Fig. 7k,m). In addition, the number of IBA1$^{+}$ cells (Fig. 7l,m), the amount of phagocytes containing myelin debris (Fig. 7n,p) and the number of crystals (Fig. 7o,p) were reduced by galunisertib-agonist treatment.

Because remyelination is impaired in aged mice, we also tested whether TGFβ increases in the brain of aged mice. However, using RT-qPCR to quantify *Tgfbl* and *Tgfb2* transcript levels in 3-month-old and 12-month-old mice, we did not detect any differences (Extended Data Fig. 7j). In addition, when aged mice were treated for 14 days with galunisertib or vehicle control, we found no beneficial effects by blocking TGFβ signalling (Extended Data Fig. 7k–p). These findings indicate that blocking TGFβ signalling efficiently promotes remyelination only in conditions associated with excessive TGFβ signalling, such as in WD-fed mice.

## Stimulating TREM2 signalling improves remyelination

Next, we were interested in understanding whether we could target a related immune checkpoint by using a different strategy. Instead of blocking microglia activation by antagonizing TGFβ, we investigated whether enhancing microglia activation by stimulating

TREM2 improves lipid clearance in demyelinating lesions[46,47]. The rationale for targeting TREM2 arises from the opposing roles of TGFβ and TREM2 in microglia activation[48]. While TGFβ promotes microglia quiescence, TREM2 signalling promotes microglia activation[48]. Such an activated state is associated with induction of transcriptional programs involved in phagocytic function and lipid metabolism[49–51]. First, we determined in primary microglia cell culture how *Trem2* expression is affected by myelin phagocytosis and detected induction of *Trem2* expression by myelin uptake, an effect that was prevented by incubation with TGFβ (Fig. 8a). Next, we analysed *Trem2* expression in demyelinating lesions and found that *Trem2* transcripts were induced in lesions of CD-fed mice from 2 to 7 dpi, but to a lesser extent in WD-fed mice (Fig. 8b). Finally, we evaluated the expression of TREM2 in myelin-loaded phagocytes using immunohistochemistry and detected higher TREM2 expression in lesions of Tgfbr2 KO mice than in control mice (Fig. 8c,d). Together, these data are consistent with the proposed role of TGFβ and TREM2 as opposing factors in microglia activation, raising the possibility that enhancing TREM2 function might support beneficial microglia activity after demyelinating injury as a proregenerative therapeutic strategy after WD feeding, and possibly also in ageing. TREM2 signalling is terminated by cleavage of a disintegrin and metalloprotease (ADAM), which releases the soluble TREM2 ectodomain (sTREM2) into the extracellular space[52,53]. We assessed TREM2 and sTREM2 levels in the unlesioned brains of young (3 months old) and old (12 months old) CD-fed and WD-fed mice and detected that age enhances TREM2 levels but also promotes its cleavage (Extended Data Fig. 8a,b). We evaluated the expression of *Trem2* at early time points of demyelination in old and young mice, in which we detected a trend towards higher levels of *Trem2* in old mice (Extended Data Fig. 8c). WD consumption had no effect on TREM2 levels or cleavage in unlesioned mice (Extended Data Fig. 8d,e). To assess TREM2 shedding after myelin-debris phagocytosis, we treated primary cultures of microglia with myelin debris and determined full-length and cleaved TREM2 by Western blotting and ELISA analyses. Surprisingly, treatment of microglia with increasing amounts of myelin debris caused a profound decrease in full-length TREM2 in microglial cell lysates (Extended Data Fig. 8f,h), while sTREM2 increased in the culture medium (Extended Data Fig. 8g-i). It is unknown why myelin-debris loading of microglia triggers TREM2 cleavage, but the consequence could be the silencing of beneficial lipid metabolic pathways necessary for disease-resolving microglia functions in the CNS. Thus, we speculated that stimulating TREM2 function could promote microglia response and lipid clearance in phagocytes. To enhance a TREM2-dependent transition into activated microglia state, we used a recently identified monoclonal antibody 4D9 (ref. [54]), which enhances TREM2 function on myeloid cells. Our previous results demonstrated 4D9's mechanism of action is via potent inhibition of TREM2 shedding, and receptor activation of phospho-SYK signalling[54]. A reformatted human effectorless Fc version of 4D9 was used to avoid confounds of off-target FcγR interactions (see Methods). To analyse the influence of 4D9 on myelin-induced TREM2 cleavage, we treated cultured cells with myelin and concomitantly incubated them with 4D9 or its isotype control. Indeed, 4D9 incubation prevented TREM2 cleavage induced by myelin-debris phagocytosis (Extended Data Fig. 8i). To understand how 4D9 could influence the LXR pathway, we evaluated the change in expression of the LXR target genes *Abcal* and *Abcgl* after myelin-debris intake. In both cases, 4D9 treatment promoted the expression of these cholesterol efflux genes after myelin uptake (Fig. 8e).

To study the effect on lipid processing and remyelination in vivo, we induced focal demyelinating lesions in the spinal cord of WD-fed mice, and concomitantly dosed mouse 4D9 effectorless antibody or an isotype control for 14 days. We performed intraperitoneal injection at 0, 3, 7 and 14 dpi with 100 mg/kg (body weight) of 4D9 to obtain sufficient concentration within the CNS in the absence of a BBB-penetrating transport vehicle on the antibody[54]. Upon study termination, animals were perfused and spinal cords collected for electron microscopy to determine lipid loading in phagocytes. We observed that the number of foam cells harbouring lipid droplets was reduced in 4D9-treated WD-fed mice as compared with control antibody-treated WD-fed mice (Fig. 8f,i). To examine whether TREM2 stimulation was also beneficial for aged-induced remyelination failure, we examined the effect of the 4D9 antibody in 12-month-old mice. Lesions were induced and mice were treated with 4D9 or an isotype control antibody for 14 and 21 days. Numerous foam cells, harbouring lipid droplets and needle-shaped cholesterol crystals, were found in animals treated with isotype control antibody. Notably, we observed a marked reduction of foam cells in 4D9-treated mice (Fig. 8g,j). Next, we determined the number of myelinated axons on semithin sections of spinal-cord lesions, which allow analyses of remyelinated axons. We found that remyelination was significantly enhanced at 21 dpi in 4D9-treated aged wild-type mice as compared with isotype controls (Fig. 8h,k). Thus, we conclude that targeting immune checkpoints controlled by TGFβ and TREM2 represent a potential therapeutic strategy to improve lesion recovery after demyelinating injury.

## Discussion

WD consumption has led to high rates of obesity and diabetes across the world and is linked to chronic diseases of the brain[55–58]. As WD affects macrophage tissue function in peripheral organs, we hypothesized that it may also influence microglia responsiveness after CNS injury. We addressed the question of how WD affects microglia function and studied its consequences on the repair processes that occur after demyelinating injury in the CNS. Surprisingly, we found that WD mimics the age-associated decline of regenerative capacity in mice. WD feeding results in impaired ability of microglia in the CNS to respond and resolve innate inflammation that occurs after myelin injury. Phagocytes accumulate excessive amounts of cholesterol-rich myelin debris, which overwhelm the phagocytic efflux capacities. In order to cope with lipid overload, phagocytes are equipped with a system of nuclear lipid receptors. These receptors function as lipid sensors that respond to cellular lipid levels and elicit gene expression changes to protect cells from lipid overload, but these pathways were dysfunctional in WD-fed mice. Stimulation of lipid processing or clearance by a LXR agonist treatment was sufficient to restore the capacity of WD-fed mice to resolve lipid accumulation in phagocytes, providing evidence that these lipid-clearance pathways are central in regulating phagocyte function during recovery from demyelinating injury. It is well known that nutritional imbalances derived from WD consumption cause chronic systemic low-grade inflammatory responses in many organs, including the hypothalamus[55]. Accordingly, we observed increased microglia density and reactivity in the white matter of WD-fed mice, and therefore expected aggravated microglia responses after demyelinating injury. Surprisingly, we found suppressed phagocyte reactivity with insufficient upregulation of activation markers in early demyelinating lesions in WD-fed mice. Microglia are well-

equipped to sense signs of tissue injury and to respond in such a way resolves and clears damage to enable a return to homeostasis[59–61]. A relatively wide range of stimuli can transform microglia from a homeostatic into a disease-associated state, in which interferon-response, lysosomal and lipid-metabolism genes are upregulated[59–61]. This transformation depends on microglia immune checkpoint mechanisms such as TREM2 and TGFβ[42,51,60]. TGFβ in the CNS is abundantly produced by astrocytes and microglia, and is fundamental to specify and maintain the homeostatic transcriptional profile of microglia[45]. We found that WD results in an upregulation of TGFβ signalling in the CNS, and as a result, the microglia response that occurs after demyelinating injury is dysfunctional. Our results show that enhanced TGFβ signalling suppresses the activation of the LXR pathway, required to clear myelin-derived cholesterol after myelin-debris phagocytosis. Deleting *Tgfbr2* in adult microglia was sufficient to restore cholesterol clearance function in WD-fed mice. The reason for enhanced TGFβ signalling in WD-fed mice is unknown, but it could possibly arise as a compensating mechanism and function as a 'brake' to prevent the incremental proinflammatory microglia activation induced by the diet. TGFβ signalling may restrain microglia activity, thereby limiting microglial responsiveness and leading to poor regeneration. Other mechanisms of how TGFβ signalling influences neurological diseases have also been proposed. For example, astrocyte-derived TGFβ accelerates disease progression in amyotrophic lateral sclerosis by interfering with the neuroprotective functions of microglia[62] and the rising level of TGFβ known to occur with aging impairs the ability of oligodendrocytes to promote remyelination[63]. In addition, TGFβ ameliorates experimental autoimmune encephalomyelitis[64], and circulating TGFβ present in the blood can promote oligodendrocytes maturation and remyelination when gaining access to the lesioned CNS[65]. Hence, it appears that TGFβ signalling can be beneficial or detrimental depending on its source and cellular target. Furthermore, effects of diet on oligodendrocytes can be diverse. Dietary cholesterol can also promote repair of demyelinated lesions[66], and high dietary fat in combination with exercise training can positively modulate myelinogenesis[67].

Large efforts have been invested in identifying strategies for promoting the generation and differentiation of OPCs into premyelinating and myelinating oligodendrocytes to enhance remyelination[68–70]. Here, we expand the spectrum of potential therapeutic strategies by uncovering central microglial checkpoint mechanisms as possible targets in promoting a reparative inflammatory response after demyelinating injury. We found that unleashing microglia activation may represent a strategy to promote proregenerative responses in these conditions. This was achieved by applying TREM2-enhancing monoclonal antibody 4D9, which stimulated microglia responsiveness leading to reduction of foam cells formation and increasing remyelination. This finding is consistent with those for another TREM2 stimulating antibody, which has recently been shown to promote remyelination in the cuprizone model of demyelination in young mice[47], and to reduce pathology in mouse models of Alzheimer's disease[71]. While TREM2 activation appears to be improve remyelination by promoting lipid clearance in toxic models of demyelination, more work is necessary to determine whether the activation of microglia is also beneficial in the context of immune-mediated models of myelin damage and neurodegeneration.

# Methods

## Mouse husbandry

All mouse procedures were carried out with approval and according to the District Government of Upper Bavaria. All C57BL/6J mice were imported from Janvier Laboratories, while B6.Cg-Lepob/J mice were imported from Jackson Laboratories. The Cx3cr1$^{CreERT2}$:R26-yfp, Tgfbr2$^{fl/fl}$ line has previously been described[47]. Littermates were always used as controls. All mice were housed at the mouse facility in the German Centre for Neurodegenerative Diseases (DZNE) in Munich in a standard, pathogen-free, 12-hour light/12-hour dark cycle. The temperature in the housing facility was kept between 20 and 22 °C with 40-60% humidity. To generate diet-induced obese mice, C57BL/6J male mice were fed either a CD (CD88137, Ssniff) or WD (TD88137, Ssniff) from 6 weeks of age and during a period of 8 to 10 weeks. To induce obesity in Cx3cr1$^{CreERT2}$:R26-yfp,Tgfbr2$^{fl/fl}$ mice, 6-week-old mice were fed a WD for 4 weeks before injection. Genotyping of the Cx3cr1$^{CreERT2}$:R26-yfp,Tgfbr2$^{fl/fl}$ line was performed in a standard PCR reaction with 5 μL of extracted DNA and the following primers: *Cx3crl* forward: 5'-CCTCTAAGACTCACGTGGACCTG-3', *Cx3crl* reverse: 5'-GACTTCCGAGTTGCGGAGCAC-3', *Cx3crl* specification: 5'-GCCGCCCACGACCGGCAAAC-3', *Tgfbr-flox* forward: 5'- TAAACAAGGT CCGGAGCCCA-3' and *Tgfbr2*-flox reverse: 5'-ACTTCTGCAAGAGGTCCC CT-3'. The amplification of the transgenic *Cx3crl* locus results in a 304-base-pair fragment. To induce recombination in Tgfbr2$^{fl/fl}$ mice, tamoxifen (T5648, Sigma-Aldrich) was dissolved in corn oil to make a solution of 20 mg/mL. The solution was protected from light and placed on a shaker to dissolve overnight at 37 °C. Eight-week-old mice were administered 200 μL of tamoxifen solution via intraperitoneal injection 3 times separated by 48 hours. For all experiments, littermates carrying the respective loxP-flanked alleles but lacking expression of Cre recombinase were used as controls. Same ratios of male and female mice were used for this part of the study.

## Special diets and pharmacological treatments

WD (for diet-induced obese mice) or CD (for 12-month-old mice) was supplemented with fenofibrate (F6020, Sigma), rosiglitazone (R2408, Sigma) and GW3965 (S2630m, Selleckchem) at a concentration of 2,000 mg fenofibrate/kg diet, 100 mg rosiglitazone/kg diet and 100 mg GW3965/kg diet. Considering an average mouse weight of 32 g and a food consumption of 4 g/day, the doses of treatment were 250 mg fenofibrate/(kg (body weight) × day), 12.5 mg rosiglitazone/(kg (body weight) × day) and 20 mg GW3965/(kg (body weight) × day). Diet containing fenofibrate/rosiglitazone was supplied to animals at the day of injection and for the whole duration of the experiment, while diet containing GW3965 was supplied from 2 days before injection and for the whole duration of the experiment. For galunisertib (HY-13226, Hycultec) treatment, 175 mg of galunisertib was first dissolved in 5 mL of DMSO and then added to 245 mL of drinking water, resulting in a concentration of 0.7 mg galunisertib/mL water. Considering an average weight of 30 g and a water consumption of 6.5 mL/day, the dose of treatment was 150 mg/(kg (body weight) × day). Control mice were administered the same dose of DMSO in the drinking water. The 4D9 antibody was sequenced and reformatted onto a human IgG1-effectorless backbone[57].

Isotype and 4D9 antibody materials were produced, characterized, and assessed for quality performed at Denali Therapeutics as reported in ref. [57]. Mice were intraperitoneally administered a dose of 100 mg/kg (body weight) of isotype control antibody or 4D9 antibody cloned into a mouse backbone at the day of LLC injection and at 3, 7 and 14 days after injection.

## Lysolecithin injections

A solution of 1% lysolecithin was prepared by mixing lysolecithin (L4129, Sigma) with sterile 1× PBS. Monastral blue (274011, Sigma-Aldrich) was added to the lysolecithin solution at a concentration of 0.03% just before use to aid with visualization of the lesion during tissue processing. Mice were anaesthetized with an intraperitoneal injection of MMF solution (0.5 mg medetomidin/kg (body weight), 5.0 mg midazolam/kg (body weight) and 0.05 mg fentanyl/kg (body weight)). Then, head fur was cut away, the eyes were protected with bepanthene cream (1578847, Bayer) and a small incision was cut to expose the skull. The mouse was positioned into a stereotactic injection apparatus by accommodating the ears and the snout into the respective holders. A small hole was drilled at the following injection coordinates (from bregma): *X*, ± 1.0 mm; *Y*, -0.1 mm). A glass capillary containing the lysolecithin-monastral blue solution was then lowered to *Z:* -1.40 mm from bregma, and 1 µL was injected at a rate of 100 nL/minute. Two minutes after the delivery of lysolecithin, the capillary was slowly retracted. The mouse was then injected with 0.05 mg buprenorphin/kg (body weight), and the skin was sutured. For the injection of lysolecithin in the spinal cord, the mice were anaesthetized as above, the mouse dorsal skin was shaved and a 3-cm incision was performed to expose the thoracic-lumbar part of the vertebral column. The dorsal muscles and connective tissue between T11 and L2 were removed, thereby exposing the spinal cord. The capillary was positioned 0.5 mm lateral to the dorsal artery and lowered 1.5 mm into the tissue. The delivery of 1 µL lysolecithin was performed at a rate of 150 nL/minute, and the retraction of the capillary was performed as stated above. Anaesthesia was terminated by a subcutaneous injection of AFN solution, containing 2.5 mg/kg (body weight) atipamezol, 1.2 mg/kg (body weight) naloxon and 0.5 mg/kg (body weight) flumazenil.

## Immunohistochemistry

To prepare samples for immunohistochemistry, mice were anaesthetized with an intraperitoneal injection of 10% ketamine/2% xylazine and perfused intracardially with 4% paraformaldehyde (PFA) with a peristaltic pump (Peri-Star PRO, World Precision Instruments). Either the brain or the spinal cord were removed, postfixed in 4% PFA overnight and cryoprotected in 30% sucrose in PBS. The tissue was embedded in Tissue-Tek O.C.T, frozen on dry ice and kept at –80 °C until sectioning. For sectioning the injected brains and spinal cords, a cryostat (CryoStar NX70, Thermo Scientific) was used to cut 16-µm-thick coronal sections, which were directly mounted on Superfrost Plus slides in a serial manner. The lesions were identified by the presence of monastral blue. For sectioning unlesioned brains, we collected 30-µm-thick sagittal sections in a cryoprotecting solution (25% glycerol, 25% ethylene glycol, in 1× PBS). All sections were kept at –20 °C until further processing. For staining the sections for lipidic antigens, the sections were first dried at 37 °C for 30 minutes, rinsed with 1× PBS and permeabilized for 10 min in 1× PBS

containing 0.3% Triton X-100. To prevent non-specific binding, sections were incubated for 1 hour with blocking solution (2.5% bovine serum albumin, 2.5% fish gelatin and 2.5% fetal calf serum in 1× PBS). Primary antibodies were diluted in staining solution (25% of blocking solution in 1× PBS) and incubated overnight at 4 °C. Then, the sections were further incubated with primary antibodies for 1 hour at RT, washed with 1× PBS, and subsequently incubated with secondary antibodies (1:1,000) for 2 hours. After washing with 1× PBS, the sections were then incubated with FluoroMyelin (1:400, F34651, Invitrogen) and DAPI (1:1,000) in 1×PBS for 15 minutes. The sections were then washed in 1× PBS in distilled water and then mounted with mowiol.

For staining the sections with non-lipidic antigens, permeabilization was performed by using 1× PBS with 1% Triton X-100 for all solutions (blocking solution, staining solution) and for washes. For stainings with antibodies produced in mice, we added a Fab fragment-blocking step (715-007-003, Jackson ImmunoResearch) before adding the blocking solution. All steps were performed at room temperature (RT) unless stated otherwise. For CC1 and TREM2 staining, heat-induced antigen retrieval was performed before blocking. For TREM2 staining, primary antibodies were incubated at RT overnight.

The primary antibodies used were the following: IBA1 rabbit (1:1000, Cat. No. 019-19741, Wako), IBA1 guinea pig (1:500, Cat. No. 234004, Synaptic Systems), MAC2 rat (1:400, Cat. No 125402, BioLegend), MHCII rat (1:100, Cat. No. 14-5321, Affymetrix-eBioscience), CLEC7A rat (1:30, Cat. No. Mabg-mdect, InvivoGen), AXL goat (1:100, Cat. No. AF854-SP, R&D Systems), pSMAD2 rabbit (1:1,000, Cat. No. AB-3349-I, Millipore), pSMAD3 rabbit (1:500, Cat. No. 600-401-919, Rockland), PLIN2 guinea pig (1:500, GP40, Progen), GFAP guinea pig (1:400 Cat. No. 173004, Synaptic Systems), ALDH1L1 mouse (1:300 Cat. No. WH0010840M1, Sigma-Aldrich), GFAP mouse (1:500, clone GA5, Cat. No. NCL-GFAP-GA5, Leica Biosystems), PLP mouse (1:250, Cat. No. MCA839G, Bio-Rad), APC-CC1 mouse (1:100, Cat. No. OP80, Merck Calbiochem), CD68 rat (1:400, Cat. No. MCA1957, Bio-Rad) zand TREM2 sheep (1:50, Cat. No. AF1729, R&D Systems). Fluorescent secondary antibodies including Alexa Fluor 488, Alexa Fluor 555 and Alexa Fluor 647 were purchased from Invitrogen and used at a concentration of 1:1,000, 1:750 or 1:500 depending on the experimental instructions. Further information on primary antibody reactivity and validation is found in the reporting summary.

### Fluorescence in situ hybridization

The RNAscope Multiplex Fluorescent v2 Assay (Advanced Cell Diagnostics Inc.) was performed according to the manufacturer's instructions for fixed frozen tissue. First, 16-μm-thick brain sections were hybridized with the respective mRNA probes: RNAscope Probe-Mm-Tgfb1, Cat. No. 407751; RNAscope Probe-Mm-Tgfb2-C2, Cat. No. 406181-C2; RNAscope Probe-Mm-Abca1, Cat. No. 522251; RNAscope Probe-Mm-Abcg1-C2, Cat. No. 422221-C2; and RNAscope Probe-Mm-Tgfbr2, Cat. No.;406241, all from Advanced Cell Diagnostics. Additionally, the negative control probe (RNAscope 3-Plex Negative Control Probe, Cat. No. 320871) and the positive control probe (RNAscope 3-plex Positive Control Probe_Mm, Cat. No. 320881) were used in some sections, to assure the specificity and the

sensitivity of the signal. The target probes were also combined with immunofluorescence for IBA1 and GFAP-ALDH1L1, in order to determine which cells express the genes of interest.

## Generation of recombinant anti-TREM2 antibodies

Generation of recombinant anti-TREM2 antibodies was performed as described in ref. [54]. Wistar rats were immunized subcutaneously (s.c.) and intraperitoneally (i.p.) with a mixture of 70 μg recombinant his-tagged mouse Trem2 protein (aa19-171, Creative Biomart) in 500 μL PBS, 5 nmol CpG2006 (TIB MOLBIOL) and 500 μL incomplete Freund's adjuvant. Fusion of the myeloma cell line P3X63-Ag8.653 with the rat immune spleen cells was performed. Hybridoma supernatants were tested in an enzyme-linked immunoassay using biotinylated peptides (0.2 μg/mL) bound to avidin-coated plates. The hybridoma cells of TREM2-reactive supernatants were cloned at least twice by limiting dilution. The IgG subclass was determined in an ELISA with mouse anti-rat kappa light chain antibodies as capture and HRP-coupled mouse anti-rat IgG subclass-specific antibodies for detection. Total RNA was extracted from the monoclonal antibody expressing hybridoma cells using QIAGEN RNeasy Plus Mini Kit (QIAGEN), following the manufacturers instructions. The extracted total RNA was used as template for 5'-RACE-ready cDNA synthesis (Takara Bio). The heavy chain variable domain (VH) and the light chain variable domain (VK) of 4D9 were amplified separately by PCR using the 5'-RACE adapter-specific forward primer, rat IgG or kappa constant-specific reverse primers. For VK domain amplification, a peptide nucleic acid oligo (CCTGTGGAGGAGGAGGATGCT-KK) was used to selectively amplify the functional kappa chain. The PCR products of VH and VK were purified and cloned into the pCR-TOPO vector (Invitrogen). The cloned vector was transformed into TOP10 *Escherichia coli* (Invitrogen) by chemical transformation and selected on a LB agar plate containing 100 μg/mL carbenicillin. Sanger sequencing was done on bacteria colonies using the M13 forward and M13 reverse primers to sequence VH and VK of the 4D9 antibody. The polypeptide sequences of VH and VK were codon optimized for CHO cell expression and synthesized by Integrated DNA Technologies (Coralville). The synthesized VH and VK fragments were cloned into the human IgG1 containing effector knock-out mutations (L234A, L235A, and P329G) and human kappa chain expression vectors, respectively. ExpiCHO cells (Gibco) were transfected with the antibody expression plasmids. The culture medium containing the expressed recombinant antibody was collected 5 days after transfection. The recombinant antibody was purified by MabSelect SURe (GE Life Sciences, Pittsburgh, PA). The purity of 4D9 recombinant antibody was analysed by SDS-PAGE (NuPAGE 4-12% Bis-Tris, Invitrogen) and size exclusion chromatography (Tosoh TSKgel, Tosoh Biosciences).

## Primary microglia cultures

Primary microglia cultures were prepared from p7-p10 C57BL/6J mouse brain. The brains were homogenized using the neural tissue dissociation kit with papain (130-092-628, Miltenyi Biotech) and the resulting homogenate was filtered through a 70-μm cell strainer to obtain a single-cell suspension. Then, $CD11b^+$ cells were labelled using magnetic beads and isolated using a magnetic column. Microglia were kept in DMEM supplemented with 10% bovine calf serum, 20% L929-conditioned media, 1% penicillin/ streptomycin and 1% glutamate for 4-7 days before using them for experiment. The non-labelled cells were




Europe PMC Funders Author Manuscripts

centrifuged at 120*g* for 5 minutes, resuspended in astrocyte medium (DMEM-F12 supplemented with 1% penicillin/streptomycin, 1% glucose, 2% B27, 10% fetal bovine serum, 10 ng/mL of epidermal growth factor and 10 ng/mL of fibroflast growth factor) and transferred into a 25 $cm^2$ flask and incubated for 5-7 days to obtain astrocyte culture. Once cells were confluent, they were deattached from the flask using 0.05% trypsin/EDTA solution, plated in 12-well plates and kept in astrocyte medium for subsequent experiments.

To analyse the influence of glucose on gene expression of TGFβ ligands, we incubated microglia for 16 hours with DMEM (41965062, Life Technologies) supplemented with 1% penicillin/streptomycin, 1% glutamate and 3 mg/mL of lipoprotein-deficient serum (LP4, Merck). Then, microglia were incubated for 4 hours with no-glucose DMEM (11966025, Life Technologies) supplemented with 1% penicillin/streptomycin, 1% glutamate and 5.5 mM of glucose. Finally, cells were incubated for 4 hours with either no-glucose-DMEM (11966025, Life Technologies) supplemented with 1% penicillin/streptomycin, 1% glutamate containing 5.5 mM or 35 mM of glucose. Microglia were then washed once with 1× PBS and collected for RNA isolation following the manufacturer's instructions of the RNeasy Plus Mini Kit (74134, Qiagen).

To evaluate the influence of lipids on gene expression of TGFβ ligands in microglia, we incubated primary microglia for 24 hours with DMEM (41965062, Life Technologies) supplemented with 1% penicillin/streptomycin, 1% glutamate and 3 mg/mL of lipoprotein-deficient serum (LP4, Merck) followed by 24 hours incubation with the same medium supplemented with or without 1% of Lipid Mix (L0288, Sigma). To evaluate the influence of lipids on gene expression of TGFβ ligands in astrocytes, we incubated primary astrocytes for 24 hours with DMEM-F12 supplemented with 1% penicillin/streptomycin, 1% glucose and 2% B27 followed by 24 hours incubation with the same medium supplemented with or without 1% of Lipid Mix (L0288, Sigma). Cells were then washed once with 1× PBS and collected for RNA isolation following the manufacturer's instructions of the RNeasy plus mini kit (74134, Qiagen).

To analyse the influence of TGFβ on the gene expression changes upon myelin treatments, the medium was removed, and the microglia washed twice with DMEM (41965062, Life Technologies). Then, microglia were cultured in DMEM supplemented with 1% penicillin/streptomycin, 1% glutamate and 3 mg/mL of lipoprotein-deficient serum (LP4, Merck) with or without TGFβ2 (100- 35B-2, PrepoTech) for 16 h. Next, purified myelin was added to the media at a concentration of 8 μg/mL for 2 hours. After being washed twice, the cells were kept for further 4 or 24 hours with the corresponding medium. Microglia were then washed once with 1× PBS and collected for RNA isolation following the manufacturer's instructions of the RNeasy plus mini kit (74134, Qiagen).

To evaluate myelin intake by microglia, $CD11b^+$ cells were plated on poly-L-lysine-coated glass coverslips. On the day of the experiment, the media was removed, and the microglia washed twice with DMEM (no. 41965062, Life Technologies). Then, microglia were cultured in DMEM (no. 41965062, Life Technologies) supplemented with 1% penicillin/streptomycin, 1% glutamate and 3 mg/mL of lipoprotein-deficient serum (LP4, Merck) with or without TGFβ2 (100-35B-2, PrepoTech) for 16 h. Next, purified myelin was added to the

medium at a concentration of 8 μg/mL for 2 hours. Then, coverslips were washed once with 1× PBS, fixed for 10 minutes in 4% PFA, permeabilized in 1× PBS with 0.1% Triton X-100 for 3 minutes, blocked using blocking solution (2.5% bovine serum albumin, 2.5% fish gelatin and 2.5% fetal calf serum in 1× PBS) for 1 hour at RT and incubated with primary antibodies against PLP (mouse, 1:200, Cat. No. MCA1957, Bio-Rad) and IBA1 (rabbit, 1:500, Cat. No. 019-19741, Wako) for 1 hour at RT in 10% blocking solution in 1× PBS. After washing three times with 1× PBS, coverslips were incubated with secondary antibodies diluted 1:750 in 10% blocking solution in 1× PBS. Finally, nuclei were counterstained with DAPI and coverslips were mounted with Mowiol.

### Bone-marrow-derived macrophage culture

For the preparation of BMDMs, the femur and tibia of 8 weeks old C57BL/6 mice were isolated and cut at the extremities. The bone marrow was flushed out with DMEM, resuspended to a single-cell suspension by repeated pipetting and passed through a 70-μm cell strainer. The cells were then plated in culture medium (DMEM (41965062, Life Technologies) supplemented with 10% fetal calf serum, 1% penicillin/streptomycin and 1% glutamate) with 20% of MCSF-enriched cell culture supernatant from the L929-cell line for at least 7 days.

To analyse the effect of 4D9 on the gene expression of the LXR targets *Abcal* and *Abcgl*, BMDMs were incubated for 24 hours with DMEM (41965062, Life Technologies) supplemented with 1% penicillin/streptomycin, 1% glutamate and 3 mg/mL of lipoprotein-deficient serum (LP4, Merck), followed by 16 hours incubation with 20 μg/ml of 4D9 cloned into a human backbone or its isotype control antibody. Myelin was then added at a concentration of 8 μg/ml for 2 hours. Subsequently, myelin was washed away with DMEM and the 4D9/ isotype control-containing medium was again added to the cells for an additional 4 hours. The cells were then washed once with 1× PBS and collected for RNA isolation following the manufacturer's instructions of the RNeasy Plus Mini Kit (74134, Qiagen).

To analyse the influence of TGFβ on the gene expression changes upon myelin treatments, the medium was removed, and the BMDMs washed twice with DMEM (41965062, Life Technologies). Then, BMDMs were cultured in DMEM supplemented with 1% penicillin/ streptomycin, 1% glutamate and 3 mg/ mL of lipoprotein-deficient serum (LP4, Merck) with or without TGFβ2 (100- 35B-2, PrepoTech) for 16 h. Next, purified myelin was added to the medium at a concentration of 8 μg/mL for 2 hours. After washing the cells twice, the cells were kept for further 4 hours with the corresponding medium. BMDMs were then washed once with 1× PBS and collected for RNA isolation following the manufacturer's instructions of the RNeasy plus mini kit (74134, Qiagen).

### Western blot analysis of primary cultures

To analyse the effect of myelin on TREM2, primary microglia were treated with myelin (5 or 30 μg/mL) or LPS (1 μg/mL) for 24 hours. Cells were collected and resuspended in RIPA buffer (150 mM NaCl, 1.0% Triton X-100, 0.5% sodium deoxycholate, 0.1% SDS, 50 mM Tris, pH 8.0). Cell lysates were cleared of cellular debris by centrifugation (15,000 r.p.m. for

5 minutes), and equal amounts of protein were separated by SDS-PAGE on 12.5% acrylamide gels and transferred to 0.45-μm nitrocellulose membranes. The membranes were blocked (3% milk and 0.05% Tween 20 in TBS), incubated with primary antibodies overnight at 4 degrees in blocking solution and washed with TBST 3 times. The membranes were then incubated with horseradish-peroxidase-conjugated secondary antibodies for 1 hour at room temperature. After being washed in TBST, the membranes were visualized using an enhanced chemiluminescence system (32106, Pierce). The antibodies used were anti-TREM2 (1:50, clone 5F4) and anti-tubulin (1:10,000, Cat. No. T6557, Sigma-Aldrich). To measure the amount of soluble TREM2, the medium of the treated cells was collected and centrifuged at 3,200*g* for 20 minutes to remove cell and myelin debris. The medium was then concentrated with Amicon Ultra-4 10 kDa Centrifugal Filter Units (UFC801024, Merck), and equal volumes were loaded on a 12.5% acrylamide gels and run as described above.

### Enzyme-linked immunosorbent assay of primary microglia

To analyse the effect of 4D9 on TREM2, primary microglia cells were pretreated with 20 μg/mL 4D9 cloned into a human backbone and the isotype control antibody for 16 hours. Myelin was then added to the cells for an additional 24 hours; the medium was then cleared of debris by centrifugation and 100 μL of the medium was collected for the ELISA. Levels of sTREM2 in conditioned medium from primary microglia upon treatment with myelin at varying concentrations and 20 μg/mL TREM2-enhancing antibody 4D9 or isotype control antibody were quantified by MSD ELISA as previously described[57]. Samples were diluted 1:4 in sample buffer (1% bovine serum albumin (BSA) and 0.05% Tween 20 in PBS pH 7.4) before loading onto the MSD plate.

### Myelin purification

Myelin was isolated as previously described[21]. Briefly, 8-week-old C57BL/6J mouse brains were homogenized by sonication in 10 mM HEPES buffer (pH 7.4). The homogenate was layered on a sucrose gradient of 0.32 M and 0.85 M sucrose and centrifuged at 25,000 r.p.m. for 38 minutes with a SW32Ti rotor (Beckman Coulter). The crude myelin fraction was carefully isolated from the interface and subjected to three rounds of osmotic shock by being dissolved in MilliQ water (ddH2O) and centrifuging, first at 25,000 r.p.m., then at 10,000 r.p.m. for 18 minutes. The resulting pellet was again laid on a sucrose gradient and the same procedure was repeated to purify myelin. The yield of myelin was calculated by measuring the total amount of protein with the Bradford assay (500–0006, Bio-Rad). Before addition to the cell culture medium, myelin was resuspended by passing the solution through a 25-G needle.

### Tissue processing for RNA, protein or sterol quantifications

To measure RNA or protein content in unlesioned brain, mice were euthanized by cervical isolation, and brains were isolated and dissected in several sections, which were then flash frozen in dry ice and kept at –80 °C until analysis. To obtain enough lesion material for downstream RNA, protein and sterol analysis, we injected lysolecithin in four different sites in the corpus callosum. The injection coordinates from the bregma were the following: *X*, ± 1.0 mm; *Y*, –0.1 mm; *Z*,–1.40 mm; and *X*, ± 0.55 mm, *Y*, –1.22 mm; *Z*, –1.40 mm. At the

desired time point, mice were euthanized by cervical dislocation and the brain was isolated. Using a vibratome (Leica Systems), we cut 400-μm sections at a speed of 1 mm/s. The lesion could be localized thanks to the monastral blue dye (274011, Sigma-Aldrich). The lesion was then further dissected using fine blades, transferred into a centrifuge tube, flash frozen in dry ice and kept at –80 °C.

### RNA isolation and RT–qPCR

Total RNA was isolated from either lesions, unlesioned brain tissue or primary microglia cultures following the manufacturer's instructions of the RNeasy plus mini kit (74134, Qiagen). The RNA was retrotranscribed with the superscript III first-strand synthesis system (18080051, Invitrogen) using 100 ng to 1 μg of total RNA. Quantitative PCR was performed using the PowerUp SYBR Green Master Mix (A25742, Applied Biosystems) on a LightCycler 480 Real-time PCR system (Roche). All qPCR reactions were run in triplicate. The primers used for qPCR were the following: *Apoe* forward 5'-CTGACAGGATGCCTAGCC3', reverse 5'-TCCCAGGGTTGGTTGCTTTG-3', *Abca1* forward 5'-TGTCTGAAAAAGGAGGACAGTG-3', reverse 5'-TGT CACTTTCATGGTCGCTG-3', *Abcg1* forward 5'- CAGACGAGAGA TGGTCAAAGA-3', reverse 5'-TCAAAGAACATGACAGGCGG-3', *Tgjb1* forward 5'-CTGCTGACCCCCACTGATAC-3', reverse 5'-AAGCCCTGT ATTCCGTCTCC-3', *Tgfb2* forward 5'-TCCCCTCCGAAAATGCCATC-3', reverse 5'-TGCTATCGATGTAGCGCTGG-3', *Tgfbr2* forward 5'-AGGAC CATCCATCCACTGAAAC-3', reverse 5'-TGTCGTTCTTCCTCCACACG-3', *Trem2* forward 5'-GACCTCTCCACCAGTTTCTCC-3', reverse 5'-TCCCATTCC GCTTCTTCAGG-3', *Prgn* forward 5'-CTGCCCGTTCTCTAAGGGTG-3', reverse 5'-ATCCCCACGAACCATCAACC-3'. For housekeeping genes, we used *Rplp0* forward 5'-AAACTGCTGCCTCACATCCG-3', reverse 5'-AGCAGC TGGCACCTTATTGG-3', and *Cyc1* forward 5'-ATGGGGAG ATGTTCATGCGG-3', reverse 5'-CTGAGGTCAGGGGGTAAGC-3'.

### Western blot of isolated lesions and microglia

To analyse the influence of WD on APOE levels, 2 and 7 dpi lesions of CD- and WD-fed mice were collected as described above and lysed in RIPA buffer (150 mM NaCl, 1.0% Triton X-100, 0.5% sodium deoxycholate, 0.1% SDS, 50 mM Tris, pH 8.0). Cell lysates were cleared of cellular debris by centrifugation (15,000 r.p.m. for 5 minutes) and equal amounts of protein were separated by SDS-PAGE on gradient acrylamide gels for 2 hours and transferred to 0.45 μm nitrocellulose membranes for 1 hour. The membrane was then boiled in TBS for 5 minutes, blocked using iBlock Tropix (T2015, Applied Biosystems) with 0.1% Tween 20 for 1 hour and incubated with primary antibodies diluted in blocking solution overnight at 4 °C. Subsequently, the membrane was washed with TBST three times and incubated with horseradish-peroxidase-conjugated secondary antibodies (1:10,000, Cat. No. W4018, Promega) diluted in blocking solution for 1 hour at room temperature. After washing in TBST, the membranes were visualized using an enhanced chemiluminescence system (32106, Pierce). The antibodies used were anti-APOE (1:2,000, Cat. No. AB183596, Abcam), anti-tubulin (1:2,000, Cat. No. T6557, Sigma-Aldrich).

To quantify protein levels of TGFβR2 in conditional Tgfbr2 KO, we isolated microglia two weeks after tamoxifen treatment. Briefly, mice were perfused for 5 minutes with ice-cold PBS, the tissue was dissociated using papain (130-092628, Miltenyi Biotech) and slow pipetting through fire-polished glass pipettes of decreasing sizes; subsequently, the solution was strained through a 70-μm strainer to obtain a single-cell suspension. Finally, microglia were incubated with $CD11b^+$ magnetic beads and isolated through a magnetic column. Isolated microglia were resuspended in RIPA buffer (150 mM NaCl, 1.0% Triton X-100, 0.5% sodium deoxycholate, 0.1% SDS, 50 mM Tris, pH 8.0). Cell lysates were cleared of cellular debris by centrifugation (15,000 r.p.m. for 5 minutes) and equal amounts of protein were separated by SDS-PAGE on 12.5% acrylamide gels and transferred to 0.45 μm nitrocellulose membranes. The membranes were blocked (3% milk and 0.05% Tween 20 in TBS), incubated with primary antibodies overnight at 4 °C in blocking solution and washed with TBST three times. The membranes were then incubated with horseradish-peroxidase-conjugated secondary antibodies for 1 hour at room temperature. After washing in TBST, the membranes were visualized using an enhanced chemiluminescence system (32106, Pierce). The antibodies used were anti-TGFβR2 (1:100, Cat. No. sc-17792, Santa Cruz) and anti-GAPDH (1:8000, Cat. No. ab9484, Abcam).

### Measurement of TGFβ1 in the demyelinated lesions

To measure total amounts of TGFβ1 in the demyelinated lesions from CD and WD mice, 2 dpi lesions were collected as described above and lysed in RIPA buffer (150 mM NaCl, 1.0% Triton X-100, 0.5% sodium deoxycholate, 0.1% SDS, 50 mM Tris, pH 8.0). Then, ELISA was performed using the kit Mouse TGFβ1 ELISA Kit (ab119557, Abcam), following the manufacturer's instructions. Equal amount of protein was loaded for all samples (30 μg). The absorbance of the microplate was read on a spectrophotometer using 450 nm as the primary wavelength and 620 nm as reference wavelength.

### Measurement of TREM2 and sTREM2 in unlesioned brain

Brain chunks from a 2-mm-thick section of a lateral hemisphere of the brain between a $Y$ coordinate of +1.0 mm and -1.0 mm relative to the bregma were pulverized using a liquid nitrogen cooled mini mortar (Z756377, Sigma). About 20 mg of brain powder were transferred to soft tissue homogenizing Precellys tubes (Bertin Technologies) on dry ice and tubes were stored at –80°C until protein extraction. Tubes were put on ice and 150 μL ice-cold DEA buffer (0.2% diethylamine, 50 mM NaCl, pH 10) supplemented with protease inhibitor (P8340, Sigma) was added to generate soluble extracts. The powder was homogenized at 6,500 r.p.m. for 30 seconds at 4 °C using a sample homogenizer (Precellys Evolution, Bertin Technologies). Upon centrifuging for 10 minutes at 5,000*g* (4°C) the supernatant was ultracentrifuged (60 minutes, 130,000*g*, 4°C) while the pellet was kept on ice. The supernatant from the ultracentrifugation (that is, DEA fraction) was collected and the pH was adjusted by adding 10% 0.5 M Tris/HCl pH 6.8. DEA fractions were stored at −80°C.

For the generation of total cellular extracts, the pellet as derived from the first centrifugation step (containing membranes, nuclei and mitochondria) was resuspended in 150 μL RIPA buffer (20 mM Tris/HCl pH 7.5, 150 mM NaCl, 2.5 mM EDTA, 1% NP-40, 1% sodium

deoxycholate, 2.5 mM sodium pyrophosphate) supplemented with protease inhibitor (P8340, Sigma) by shaking briefly at 4°C. The tissue was then homogenized at 5,000 r.p.m. for 30 seconds at 4°C (Precellys Evolution, Bertin Technologies). Samples were centrifuged for 10 minutes at 5,000*g* (4°C) to remove insoluble material, and the supernatant was subjected to ultracentrifugation (60 minutes, 130,000*g*, 4°C). The supernatant (that is, the RIPA fraction) was collected and stored at -80°C.

Total protein concentrations in DEA and RIPA fractions were determined using the BCA assay (Interchim), and TREM2 levels were quantified employing a previously described MSD ELISA-based protocol[72]. MSD small spot streptavidin plates (L45SA-1) were used. The standard (recombinant murine Trem2, Hölzel Diagnostika) was diluted in either DEA buffer (with 10% 0.5 M Tris/HCl pH 6.8 added) or RIPA buffer. On the MSD plate, standard and DEA/RIPA samples were diluted 1:2 with sample dilution buffer (1% BSA, 0.05% Tween 20 in PBS pH 7.4) supplemented with protease inhibitor (Sigma, P8340). For DEA and RIPA extracts, the standard was spanning concentrations from 2,000 to 31.25 pg/mL and from 500 to 7.81 pg/mL, respectively. Trem2 concentrations as determined in pg/mL were converted in fg/μg total protein; 45 μg and 13 μg total protein was loaded for DEA and RIPA fractions, respectively.

## Sterol quantification

Sterols and oxysterols were extracted from isolated lesions by chloroform/methanol (1/1; v/v), dried under nitrogen and the residual sterols/ oxysterols were silylated to their corresponding trimethylsilylethers. Cholesterol precursors such as lathosterol, lanosterol, dihydro-lanosterol and desmosterol, together with the cholesterol metabolite 5a-cholestanol and the phytosterols, campesterol and sitosterol, were determined by gas chromatography-mass spectrometry selected ion monitoring (GC-MS-SIM), using epicoprostanol as internal standard. 24S- and 27-hydroxycholesterol were measured by isotope dilution mass spectrometry[73,74]. Data are given as amount of oxysterol/cholesterol per whole sample volume.

## Annotation of lipid classes and species

Glycerolipids are referred to as triacylglycerols (TAG) and diacylglycerols (DAG); glycerophospholipids and lyso-glycerophospholipids to phosphatidic acids (PA), phosphatidylinositols (PI), phosphatidylserines (PS), phosphatidylglycerols (PG), phosphatidylethanolamines (PE), phosphatidylcholines (PC), ether phosphatidylethanolamines (PE O-), ether phosphatidylcholines (PC O-), lyso-phosphatidic acids (LPA), lyso-phosphatidylinositols (LPI), lyso-phosphatidylcholines (LPC) and lyso-phosphatidylethanolamines (LPE); sphingolipids to ceramides (Cer) and sphingomyelins (SM); sterols to cholesterol (Chol) and cholesterylesters (CE). Lipid species are annotated according to their molecular composition as follows: [lipid class]-[sum of carbon atoms in LCB and FAs]:[sum of double bonds in LCB and FAs];[sum of hydroxyl groups in LCB and FA] (for example, EOS 70:3;2 denotes omega-hydroxy-shpingosine with a total length of its LCB and FA of 70; with 3 double bonds and 2 hydroxylations in total). For lipid subspecies, the individual acyl chain composition according to the same rule is given (for example

18:1;0_24:2;0), with the first entity denoting a sphingoid base (LCB) and the second a fatty acid (FA), in case of ceramides.

### Lipid extraction for mass spectrometry lipidomics

To obtain plasma for lipidomics analysis, we collected the blood from the heart using an EDTA-coated 1 mL syringe attached to a 25-G needle, which we introduced directly into the left ventricle of the heart. The blood was then transferred into an EDTA-coated tube and centrifuged at 2,000*g* for 10 minutes at 4°C to obtain plasma. We collected all plasma possible and flash-froze it in liquid nitrogen. For lipidomics analysis of white and grey matter of the brain, mice were perfused with sterile PBS for 3 minutes. Then, the brain was isolated and transferred into a glass dish with PBS. Under a stereoscope, the white and grey matter were dissociated using a combination of forceps and blades. Finally, the tissue was weighed and homogenized in PBS at a concentration of 5 mg/mL using a Dounce homogenizer. The solution was snap-frozen in liquid nitrogen and kept at -80°C until downstream analysis. Mass-spectrometry-based lipid analysis was performed by Lipotype, as described elsewhere[75]. Lipids were extracted using a two-step chloroform/methanol procedure[76]. Samples were spiked with internal lipid standard mixture containing: cardiolipin 16:1/15:0/15:0/15:0 (CL), ceramide 18:1;2/17:0 (Cer), diacylglycerol 17:0/17:0 (DAG), hexosylceramide 18:1;2/12:0 (HexCer), lyso-phosphatidate 17:0 (LPA), lyso-phosphatidylcholine 12:0 (LPC), lyso-phosphatidylethanolamine 17:1 (LPE), lyso-phosphatidylglycerol 17:1 (LPG), lyso-phosphatidylinositol 17:1 (LPI), lyso-phosphatidylserine 17:1 (LPS), phosphatidate 17:0/17:0 (PA), phosphatidylcholine 17:0/17:0 (PC), phosphatidylethanolamine 17:0/17:0 (PE), phosphatidylglycerol 17:0/17:0 (PG), phosphatidylinositol 16:0/16:0 (PI), phosphatidylserine 17:0/17:0 (PS), cholesterol ester 20:0 (CE), sphingomyelin 18:1;2/12:0;0 (SM), triacylglycerol 17:0/17:0/17:0 (TAG) and cholesterol D6 (Chol). After extraction, the organic phase was transferred to an infusion plate and dried in a speed vacuum concentrator. Dry extract from the first step was resuspended in 7.5 mM ammonium acetate in chloroform/methanol/propanol (1:2:4, v:v:v) and dry extract from the second step in 33% ethanol solution of methylamine in chloroform/methanol (0.003:5:1; v:v:v). All liquid handling steps were performed using Hamilton Robotics STARlet robotic platform with the Anti Droplet Control feature for organic solvents pipetting.

### MS data acquisition

Samples were analysed by direct infusion on a QExactive mass spectrometer (Thermo Scientific) equipped with a TriVersa NanoMate ion source (Advion Biosciences). Samples were analysed in both positive and negative ion modes with a resolution of $R_{m/z=200}$ = 280,000 for MS and $R_{m/Z=200}$ = 17,500 for MS/MS experiments, in a single acquisition. MS/MS was triggered by an inclusion list encompassing corresponding MS mass ranges scanned in 1-Da increments. Both MS and MS/MS data were combined to monitor CE, DAG and TAG ions as ammonium adducts; PC, PC O-, as acetate adducts; and CL, PA, PE, PE O-, PG, PI and PS as deprotonated anions. MS only was used to monitor LPA, LPE, LPE O-, LPI and LPS as deprotonated anions; Cer, HexCer, SM, LPC and LPC O- as acetate adducts and cholesterol as ammonium adduct of an acetylated derivative.

### MS data analysis and postprocessing

Data were analysed with in-house developed lipid identification software based on LipidXplorer[77]. Data postprocessing and normalization were performed using an in-house developed data-management system. Only lipid identifications with a signal-to-noise ratio >5, and a signal intensity fivefold higher than in corresponding blank samples were considered for further data analysis. Data were transformed to mol % per sample for each lipid, allowing the direct comparison of samples with different total lipid amounts[78]. The amounts of the lipid classes may be normalized to the total lipid amount yielding mol % per total lipids in the sample, which we refer to as ‘mol% of the sample occupied by’ in our figures.

### Glucose tolerance test

To evaluate blood glucose levels, mice were fasted for 6 hours in a quiet environment. Then, basal blood glucose levels were assessed by collecting a small drop of blood from the tail onto a Freestyle lite test strip (7081470, Abbott) and immediately measuring glucose levels with a glucometer (FreeStyle Freedom Lite, 20776-101, Abbott). Next, an intraperitoneal dose of 1.5 g glucose/kg (body weight) was given to the mice, and their blood glucose levels were repeatedly measured at 15, 30, 60 and 120 minutes after glucose administration.

### Assessment of blood–brain barrier integrity

To evaluate the effect of WD on BBB integrity, we injected CD- and WD-fed mice with 200 µl (2% v/v% in saline) of fluorescently labelled Evans blue dye (E2129, Sigma-Aldrich) intraperitoneally. After 24 hours, mice were anaesthesized and perfused with 1× PBS followed by 4% PFA. Then, their brains were isolated, postfixed overnight with 4% PFA and sectioned using a vibratome at a thickness of 100 µm. Then, the sections were mounted and the whole sections were imaged using an epifluorescence microscope (DMI6000B, Leica Microsystems) and evaluated for Evans blue presence using Fiji.

### Electron microscopy

For electron microscopy (EM), mice were intracardially perfused with 4% paraformaldehyde for 5 minutes. Then, the brain or spinal cord were dissected and postfixed in EM fixative (2% paraformaldehyde, 4% glutaraldehyde, 2 mM CaCl in 0.1 M cacodylate buffer). For better infiltration of the tissue with fixative, 200-µm-thick sections were cut with a vibratome either freshly or after one day in fixative. For vibratome sectioning of the spinal cord, the tissue was embedded in 15% gelatin to obtain more stability. Two days after perfusion, the EM fixative was washed away with 0.1 M cacodylate buffer. Then, the region of interest was isolated by punching a 1.5-mm-wide circle or cutting a 2 mm × 2 mm square. In cases where the region of interest was a demyelinated lesion, the lesion was recognized thanks to the monastral blue injected together with lysolecithin. Finally, the region of interest was wrapped in a small square of filter paper (from a tea bag) and inserted into the moulds for automatic tissue processing. Lesion samples were processed in a tissue processor (Lynx, Science Services) starting with washes in 0.1 M sodium cacodylate buffer and postfixation in reduced osmium (2% osmium, 2.5% potassium ferrocyanide in 0.1 M cacodylate buffer; Science Services). After several washing steps, the samples were en bloc

uranyl acetate contrasted (1% aqueous uranyl acetate), dehydrated, infiltrated and embedded in EPON resin (Serva). The samples were flat embedded into gelatin capsules (Science Services) and cured for 48 h at 60°C. Blocks were sectioned on a Leica UC7 ultramicrotome using a 35° Ultra Diamond Knife (Diatome) at thicknesses of 50 nm for TEM, 100 nm for SEM and 200 nm sections for light microscopy. The latter were stained using a methylene blue and azur blue stain mixed in equal amounts. Sections were imaged on a slide scanner with a 40× objective (Pannoramic MIDI II 2.0.5). Subsequently, foam cells were quantified by manual counting and normalized to the lesion area. To quantify lipid droplets in the ventricle wall, green-labelled, circular structures were manually counted and normalized to ventricle length. For scanning EM, sections were collected onto plasma-treated CNT tape (Science Services) and mounted onto 4-inch silicon wafers (Siegert Wafer) using adhesive carbon tape (Science Services). For grounding, we attached additional adhesive carbon tape strips (Science Services) between CNT tape and wafer. EM micrographs were acquired on a Crossbeam Gemini 340 SEM (Zeiss) with a four-quadrant backscatter detector at 8 kV. In ATLAS5 Array Tomography (Fibics), the wafer area was scanned at 3,000 nm/ pixel to generate an overview map. The entire section areas were scanned at 50 × 50 $nm^2$, and the lesion area at 10 × 10 $nm^2$. To quantify the amount of foam cells in the lesions in old mice treated with 4D9 or IgG isotype control, the number of foam cells was manually counted using Fiji and normalized to the lesion area. In the case of WD-fed mice treated with 4D9 or isotype control, it was harder to distinguish one foam cell from another, thus, the area occupied by lipid-droplet-, myelin-debris-containing cells was quantified using Fiji and normalized to the lesion area. To quantify remyelination, the number of axons surrounded by a thin myelin sheath was manually counted and normalized to the lesion area.

## Confocal microscopy

Optical sections were acquired with a confocal laser-scanning microscope (Leica TCS SP5, Leica Microsystems) using the 20×Air/0.75 NA and the 63×Oil/1.40 NA objectives. The *z*-step in *z*-stacks was kept at 1 μm. The different fluorophores were stimulated sequentially using the following laser lines: 405 nm for DAPI, 488 nm for Alexa Fluor 488 (AF488), 561 nm for Alexa Fluor 555 (AF555) and 633 nm for Alexa Fluor 647 (AF647). To image the cholesterol crystals, we imaged the reflected light using the same confocal microscope in parallel to the imaging of the fluorophores as previously described[79].

## Image analyses

To quantify the demyelination volume and the $IBA1^+$ volume, the area of demyelination shown by negative FluoroMyelin staining and the area of clustered $IBA1^+$ cells, respectively, was measured in consecutive sections of a lesion, which were separated by a known distance. The lesion volume was then calculated according to the truncated cone volume formula in an automated fashion using IPython 2.7. The code is available at https://github.com/lenkavaculciakova/lesion_volume. For the quantification of myelin-loaded $IBA1^+$ cells, crystal-loaded $IBA1^+$ cells, $MAC2^+IBA1^+$ cells, $MHCII^+IBA1^+$ cells, $CC1^+$ cells and foam cells, the cells were counted manually in high magnification images of the lesion using the Cell Counter plug-in in Fiji[80]. The pictures were coded so that the analysis would be blinded. For analysis of pSMAD2 staining, the percentage area of the lesion occupied by pSMAD2 staining was quantified in an automated fashion using Fiji. The

quantifications of microglia density, lipid-loaded microglia, lipid droplets lining the ventricle, CLEC7A$^+$ microglia, AXL$^+$ microglia and MAC2$^+$ microglia were performed by counting manually in tile scans of the corpus callosum. To analyse the colocalization of PLIN2$^+$ signal within IBA1$^+$ or GFAP$^+$ cells, the PLIN2 signal was overlapped with the IBA1 or GFAP signal and the percentage area covered by the overlap was quantified in an automated fashion using Fiji in tile scans of the corpus callosum. To quantify the PLIN2$^+$ signal within CD68$^+$ cells and the TREM2$^+$ signal within FluoroMyelin$^+$ signal, the PLIN2$^+$ and TREM2$^+$ signals were overlapped with CD68 and FluoroMyelin, respectively, and the percentage area covered by the overlap was quantified in high-magnification images of the demyelinated lesion in an automated fashion using Fiji. To quantify pSMAD2 or pSMAD3 signal within microglia, the pSMAD2/pSMAD3$^+$ signal was overlaid on a microglia marker (IBA1 or CD68) and quantified in either lesion or unlesioned samples in an automated fashion using FIJI. To quantify the myelin particles within microglia cells in culture, PLP$^+$ particles were overlapped with the IBA1$^+$ signal and counted in an automated way using CellProfiler. For the quantification of the *Tgfbl* and *Tgfb2* mRNA particles in the fluorescence in situ hybridization, the positive particles were quantified either in the area of interest or in the mask created by the IBA1$^+$ or GFAP$^+$ALDH1L1$^+$ signal in an automated fashion using Fiji.

## Statistics and reproducibility

Statistical analysis was performed with GraphPad Prism (GraphPad Software) and Microsoft Office Excel 2016 (Microsoft). The number of animals and cell cultures used for the experiments are indicated as single dots in all graphs or indicated in the figure legends. Normality tests confirmed the normal distribution of our data. Thus, to compare two groups, a two-tailed Welch's *t*-test was applied. For comparison of more than two groups, one-way Brown-Forsythe and Welch ANOVA followed by Dunnett's T3 multiple-comparisons post hoc test was performed. For comparing the interference between two variables, we used two-way ANOVA followed by Sidak test for multiple-comparison correction. For measuring statistical differences in RT-qPCR results, the — $2^{\Delta\Delta Ct}$ value was employed and the — $2^{\Delta\Delta Ct}$ values were subjected to the test. A $P$ value of ≤0.05 was considered significant in all cases. The analysis of the influence of WD on weight gain and recovery from demyelination was replicated in three independent experiments. For all other in vivo experiments, at least three biological replicates were used. For histological analyses depicted in Figs. 1h-i,k,n-o, 2c, 3c,f-g,j,l-m, 4g,h, 5h,p-s, 7i and 8d,i-k and Extended Data Figs. 2t, 3h, 4h and 5a,b,k, three to five random region of interests for each brain section and three to five brain sections were quantified per mouse to account for variability within the biological sample. For in vitro experiments, each experiment was replicated three or four times. For each biological replicate, three technical replicates were averaged to obtain the value used for statistical analysis. An exception is Extended Data Fig. 8f-i in which results are shown for one replicate.

Europe PMC Funders Author Manuscripts

## Extended Data

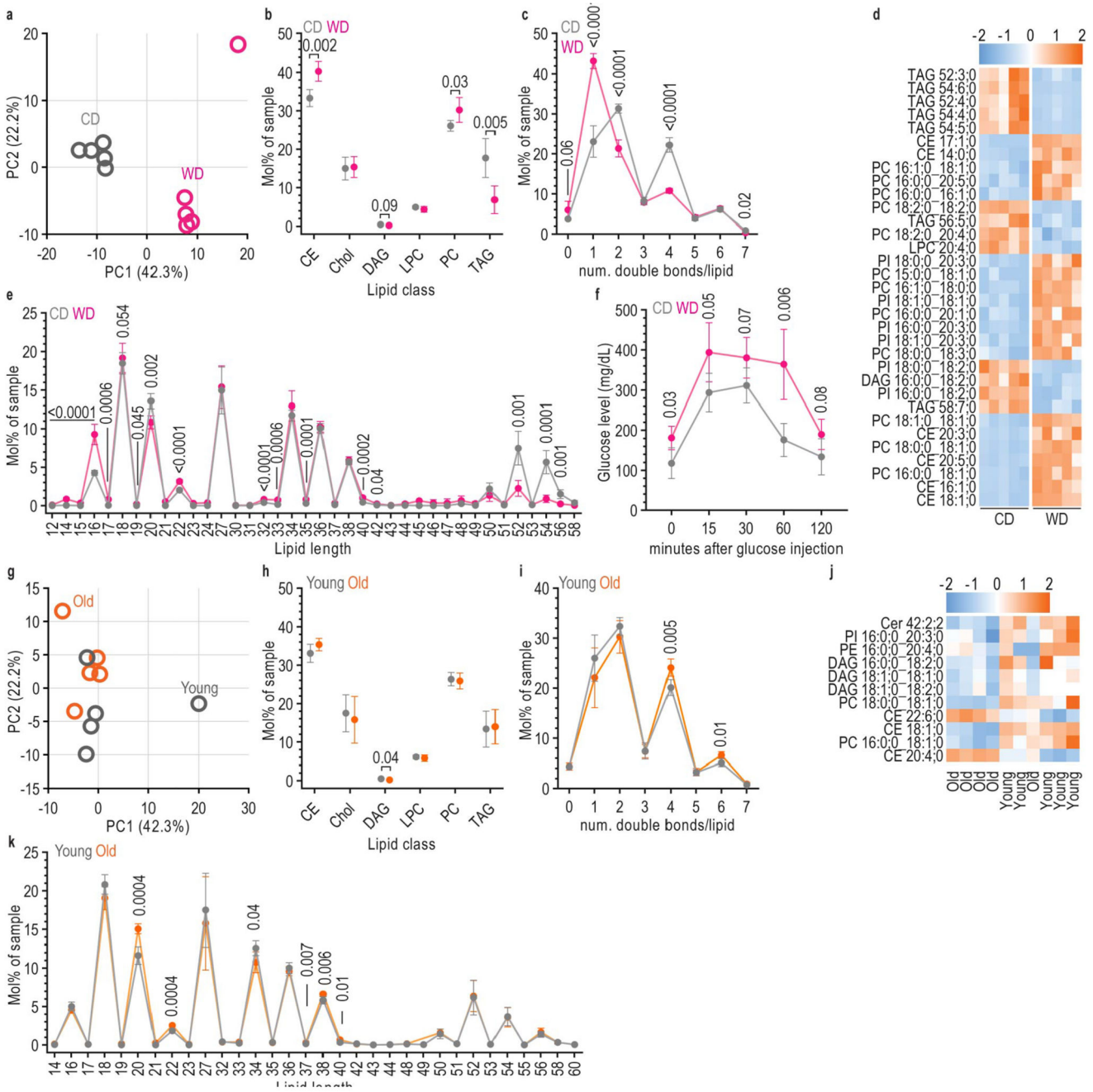


**Extended Data Fig.1. The plasma lipidome is altered by Western diet.**

**a**, PCA analysis of CD and WD plasma samples. **b**, Mol% of the sample occupied by the different lipid classes in CD- and WD-fed mice (mean±SD, two-tailed Welch's t-test). **c,e**, Mol% of each sample with lipids containing a certain number of double bonds (**c**) or a certain acyl chain length (**e**) (mean±SD, two-tailed Welch's t-test). **d**, Heatmap showing the significantly (p value ≤ 0.01, fold ≥2.5) changed lipid species in plasma from CD- and WD-

fed mice. Scale indicated on top of the heatmap. Increased values are indicated in orange, while decreased values are in blue. **f**, Quantification of the glucose level in blood at baseline (0 minutes) and 15, 30, 60 and 120 minutes after intraperitoneal glucose administration. (mean±SD, two-tailed Welch's t-test). **g**, PCA analysis of plasma from young (3-months old) versus old (12-months old) mice. **h**, Mol% of the sample occupied by the different lipid classes in plasma from young and old mice (mean±SD, two-tailed Welch's t-test). **i,k**, Mol% of each sample with lipids containing a certain number of double bonds (**i**) or a certain acyl chain length (**k**) in plasma from young and old mice (mean±SD, two-tailed Welch's t-test). **j**, Heatmap showing the significantly (p value ≤ 0.05, fold ≥1.3) changed lipid species in plasma from young and old mice. Scale indicated on top of the heatmap. Increased values are indicated in orange, while decreased values are in blue. P-values below 0.1 and n numbers are indicated in the figures. PCA: principal component analysis, CD: control diet, WD: Western diet, CE: cholesterol esters, Chol: cholesterol, DAG: diacylglycerol, LPC: lysophosphatidylcholine, PC: phosphatidylcholine, TAG: triacylglycerides, PI: Phosphatodylinositol. In d and j, the lipids are numbered according to the carbon length; number of double bonds; and number of hydroxyl groups (for example TAG 52;3;0).

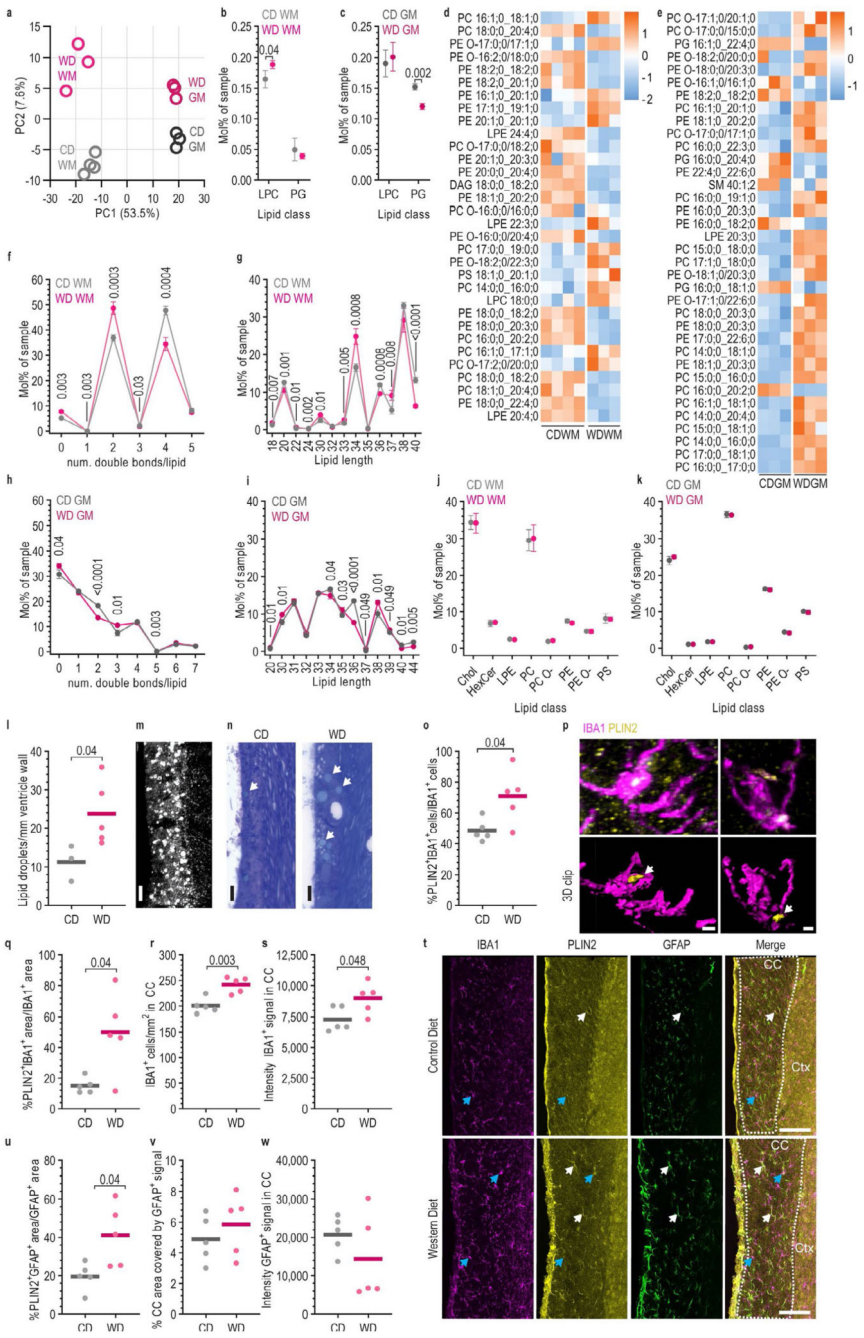

**Extended Data Fig.2. Western diet feeding alters the brain lipidome of mice.**

**a**, PCA analysis of white matter (WM) and grey matter (GM) samples from brain of WD- and CD-fed mice. **b,c**, Lipid classes changed in brain WM (**b)** and GM (**c**) between CD- and WD-fed mice (n = 3 for WD WM, CD GM and WD GM. N = 4 for CD WM, data represent mean±SD, two-tailed Welch's t-test). **d,e**, Heatmap showing the significantly (p value ≤ 0.5, fold ≥1.3) changed lipid species in the brain WM (**d**) and in the brain GM (**e**). Scale indicated on the right side of the heatmap. Increased values are indicated in orange, while decreased values are in blue. **f,g**, Mol% of each sample with lipids containing a certain





Europe PMC Funders Author Manuscripts

number of double bonds (**f**) or a certain acyl chain length (**g**) (mean±SD, two-tailed Welch's t-test). The data is shown for those lipid species significantly (p value ≤ 0.05, fold ?1.3) changed in the WM (n = 3 for WD WM, n = 4 for CD WM, data represent mean± SD, two-tailed Welch's t-test). **h,i**, Mol% of each sample with lipids containing a certain number of double bonds (**h**) or a certain acyl chain length (**i**). The data is shown for those lipid species significantly (p value ≤ 0.05, fold ?1.3) changed in the GM (n = 3 for both groups, data represent mean±SD, two-tailed Welch's t-test). **j,k**, Mol% of the sample occupied by the different lipid classes in the brain WM (**j**) and GM (**k**) in CD- and WD-fed mice (mean±SD, two-tailed Welch's t-test). **l**, Quantification of the number of lipid droplets detected in the ventricle wall separating the corpus callosum from the lateral ventricles (solid lines indicate the mean, two-tailed Welch's t-test).**m**, Representative image of a PLIN2 staining in the ventricle wall demonstrating the accumulation of lipid droplets in this structure. Scale bar: 5μm. **n**, Images of the ventricle wall separating the corpus callosum from the second ventricle in CD- and WD-fed mice. Lipid droplets are labelled in pale green and marked with white arrows. Scale bar: 5μm. **o**, Quantification of the percentage of $IBA1^+$ cells containing $PLIN2^+$ lipid droplets in the corpus callosum (solid lines indicate the mean, two-tailed Welch's t-test). **p**, Example images of microglia containing $PLIN2^+$ lipid droplets in their cytoplasm. On the top row, the raw image is displayed. On the bottom row, a 3D clip of the corresponding image is displayed, where the $PLIN2^+$ signal inside the cell is indicated with a white arrow. Scale bar images left side: 3μm, Scale bar images right side: 2μm. **q**, Quantification of the percentage of $IBA1^+$ area occupied by $PLIN2^+$ signal (solid lines indicate the mean, two-tailed Welch's t-test). **r**, Quantification of microglia density in the corpus callosum (solid lines indicate the mean, two-tailed Welch's t-test). **s**, Measurement of $IBA1^+$ signal intensity in the corpus callosum (two-tailed Welch's t-test). **t**, Images of the corpus callosum (CC) and cortex (Ctx) stained with IBA1 to label microglia, GFAP to label astrocytes and PLIN2 to label lipid droplets. White arrows indicate lipid droplets within $GFAP^+$ cells; blue arrows indicate lipid droplets within $IBA1^+$ cells. Scale bar: 100 μm. **u**, Quantification of the percentage of $GFAP^+$ area occupied by $PLIN2^+$ signal (solid lines indicate the mean, two-tailed Welch's t-test). **v,w**, Area (**v**) and intensity (**w**) of $GFAP^+$ staining in the corpus callosum of CD- and WD-fed mice. P-values below 0.1 and n numbers are indicated in the figures; each dot represents one mouse. PCA: principal component analysis, CD: control diet, WD: Western diet, WM: white matter, GM: grey matter, LPC: lysophosphatidylcholine, PG: phosphatidylglycerol, PC: phosphatidylcholine, PE: phosphatidylethanolamine, PE O-: Phosphatidylethanolamine-ether, LPE: lysophosphatidylethanolamine, DAG: diacylglycerol, PC O-: Phosphatidylcholine-ether, PS: phosphatidylserine Ctx: cortex, CC: corpus callosum, PLIN2: Perilipin2. In d and e, the lipids are numbered according to the carbon length; number of double bonds; and number of hydroxyl groups (for example LPE 24;4;0).

Europe PMC Funders Author Manuscripts

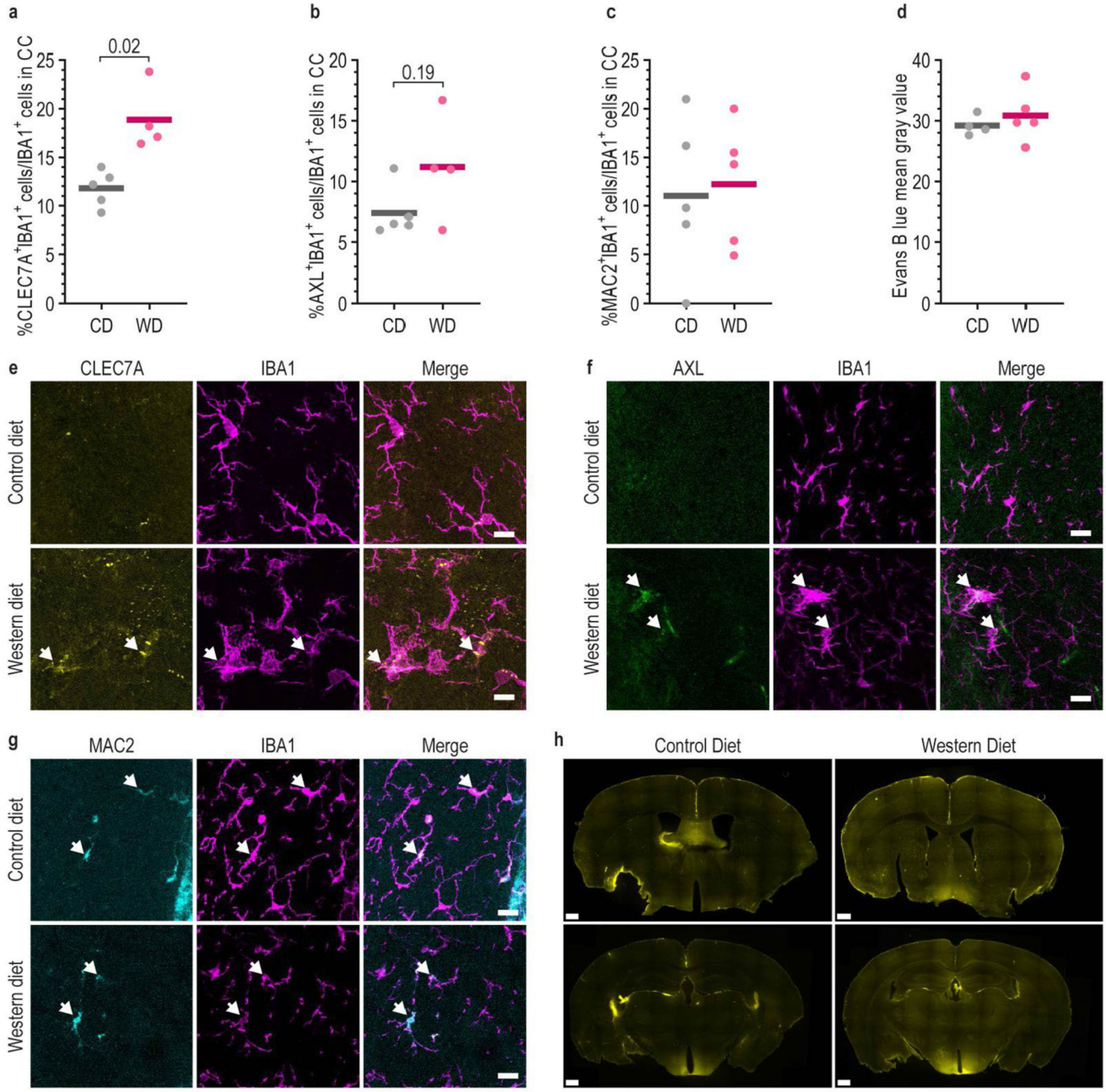


**Extended Data Fig.3. Western diet consumption causes weak microglia activation.**

**a-c**, Quantification of the percentage of CLEC7A$^+$/IBA1$^+$ (**a**), AXL$^+$/ IBA$^+$ (**b**) and MAC2$^+$/ IBA1$^+$ (**c**) cells over all the population of IBA1$^+$ cells (solid lines indicate the mean, two-tailed Welch's t-test). **d**, Quantification of the mean grey value of fluorescently labelled Evans Blue in whole brain sections of CD- and WD-fed mice (solid lines indicate the mean, two-tailed Welch's t-test). **e-g** Images of microglia in the corpus callosum labelled with IBA1 and the activation markers CLEC7A (**e**), AXL (**f**) and MAC2 (**g**). White arrows indicate cells positive for both IBA1 and the corresponding activation marker. Scale bars:

CLEC7A: 10μm, AXL and MAC2: 20μm. **h**, Images of two whole brain sections of CD- and WD-fed mice demonstrating the presence of fluorescently-labelled Evans Blue in the brain. Scale bar: 500 μm. P-values below 0.1 and n numbers are indicated in the figure; each dot represents one mouse. CD: control diet, WD: western diet.

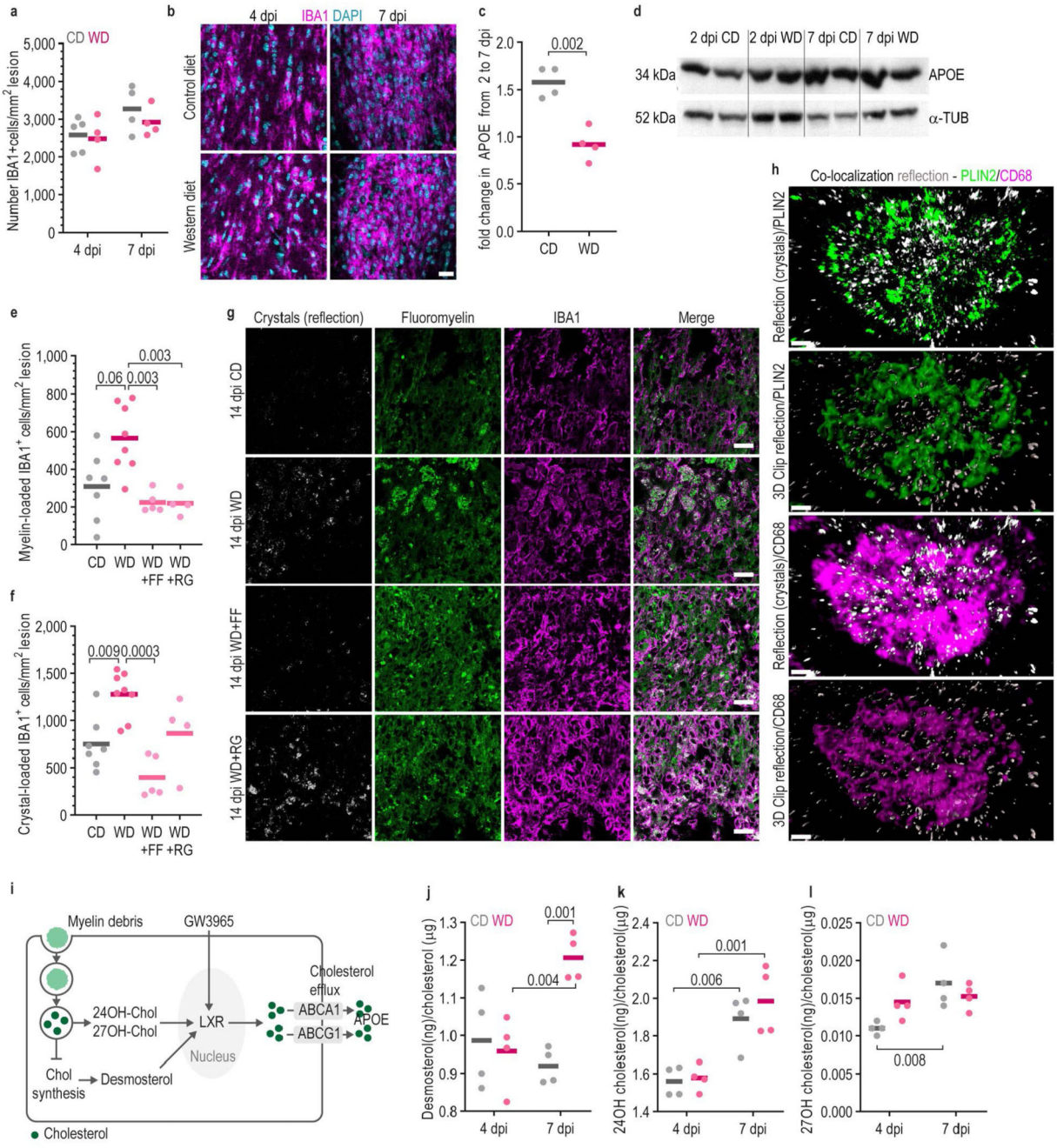


**Extended Data Fig.4. The differential production of endogenous LXR ligands does not explain the poor induction of the LXR pathway observed in WD-fed mice.**

**a**, Quantification of IBA1$^+$ cell density in the demyelinated lesions at 4 and 7 dpi in CD- and WD-fed mice. **b**, Images demonstrating the density of IBA1$^+$ cells in demyelinated lesions

Europe PMC Funders Author Manuscripts

at 4 and 7dpi. Scale bar: 20μm. **c**, Quantification of the increase in APOE levels from 2 to 7 dpi in CD- and WD-fed mice (two-tail Welch's t-test). **d**, Example images of the Western blots used for quantification of APOE levels. Molecular weights are indicated on the left side. APOE levels were normalized to α-TUBULIN (α-TUB). **e,f**, Quantification of the number of myelin- (**e**) and crystal- (**f**) loaded $IBA1^+$ cells per $mm^2$ in lesion of CD-, WD-, WD + FF- and WD+ RG-fed mice. FF and RG treatments successfully promoted myelin clearance by phagocytes in WD-fed mice (one-way Brown-Forsythe and Welch ANOVA tests with multiple comparisons corrected by Dunnett T3 test). The references groups, CD and WD, are from Fig. 4e,f. **g**, Images of the demyelinated lesion in the corpus callosum at 14dpi exemplifying myelin- and crystal-loaded $IBA1^+$ cells in all treatment groups. Scale bar: 20μm. **h**, Images demonstrating the co-localization of the cholesterol crystal signal obtained by reflection microscopy with either PLIN2 (green) or CD68 signal (magenta). Original images and 3D clips are shown. Scale bar: 2 μm. **i**, Diagram illustrating the production of the various natural liver X receptor (LXR) ligands measured in our assay. **j-l**, Quantification of the amounts of the endogenous LXR agonists desmosterol (**j**), 24-hydroxycholesterol (**k**) and 27-hydroxycholesterol (**l**) in the demyelinated lesions at 4 and 7dpi in CD- and WD-fed mice. Each LXR ligand was normalized to the cholesterol amounts in the same lesion (two-way ANOVA followed by multiple comparisons correction with Sidak test). Solid lines in the graphs indicate the mean. P-values below 0.1 and n numbers are indicated in the figure; each dot represents one mouse. dpi: days post injection, CD: control diet, WD: Western diet, α-TUB: α-tubulin, Chol: cholesterol, FF: Fenofibrate, RG: rosiglitazone.

Europe PMC Funders Author Manuscripts

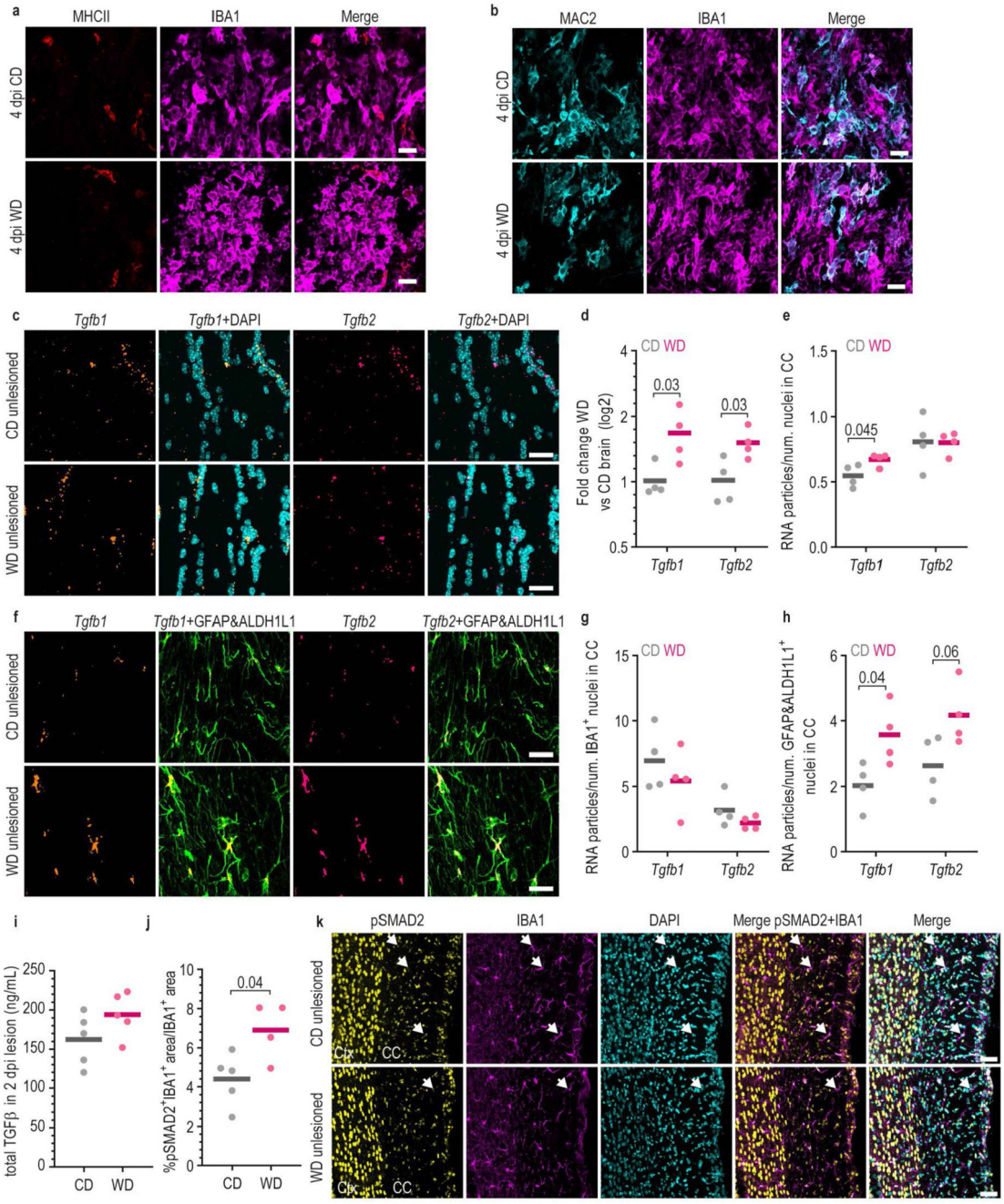


**Extended Data Fig.5. TGFβ signaling is increased in the unlesioned brain of WD-fed mice.**

**a,b**, Overview images of MHCII$^{+}$IBA1$^{+}$ (**a**) and MAC2$^{+}$IBA1$^{+}$(**b**) cells in the demyelinated lesions at 4dpi. Scale bar: 20μm. **c**, Images of the unlesioned corpus callosum of CD- and WD-fed mice demonstrating the accumulation of *Tgfb1* and *Tgfb2* particles visualized by RNA *in situ* hybridization. Scale bar: 20μm. **d**, Fold change in *Tgfb1* and *Tgfb2* expression in the brain of WD-fed mice relative to CD-fed mice (two-tailed Welch's t-test). **e**, Quantification of the number of RNA particles of *Tgfb1* and *Tgfb2* per nuclei in the corpus callosum in CD- and WD-fed mice (two-tailed Welch's t-test). **f**, Images of the unlesioned

corpus callosum of CD- and WD-fed mice demonstrating the *Tgfb1* and *Tgfb2* particles accumulating within GFAP&ALDH1L1$^+$ cells in the unlesioned corpus callosum of CD- and WD-fed mice. Scale bar: 20μm. **g,h**, Quantification of the number of *Tgfb1* and *Tgfb2* particles within IBA1$^+$ (**g**) or GFAP&ALDH1L1$^+$ cells (**h**) in the unlesioned corpus callosum of CD- and WD-fed mice (two-tailed Welch's t-test). **i**, Quantification using ELISA of TGFβ1 in the 2 dpi lesions in CD and WD mice. No significant differences were observed (p = 0.14, two-tailed Welch's t-test). **j**, Quantification of the pSMAD2$^+$ area within IBA1$^+$ area in the unlesioned corpus callosum (two-tailed Welch's t-test). **k**, Images of the unlesioned CC of CD- and WD-fed mice demonstrating accumulation of pSMAD2$^+$ signal within IBA1$^+$ cells. White arrows point to IBA1$^+$ cells accumulating low amounts of pSMAD2$^+$ signal within their nucleus. Scale bar: 40 μm. Solid lines in the graphs indicate the mean. P-values below 0.1 and n numbers are indicated in the figure. dpi: days post injection, CD: control diet, WD: Western diet. CC: corpus callosum, Ctx: cortex.

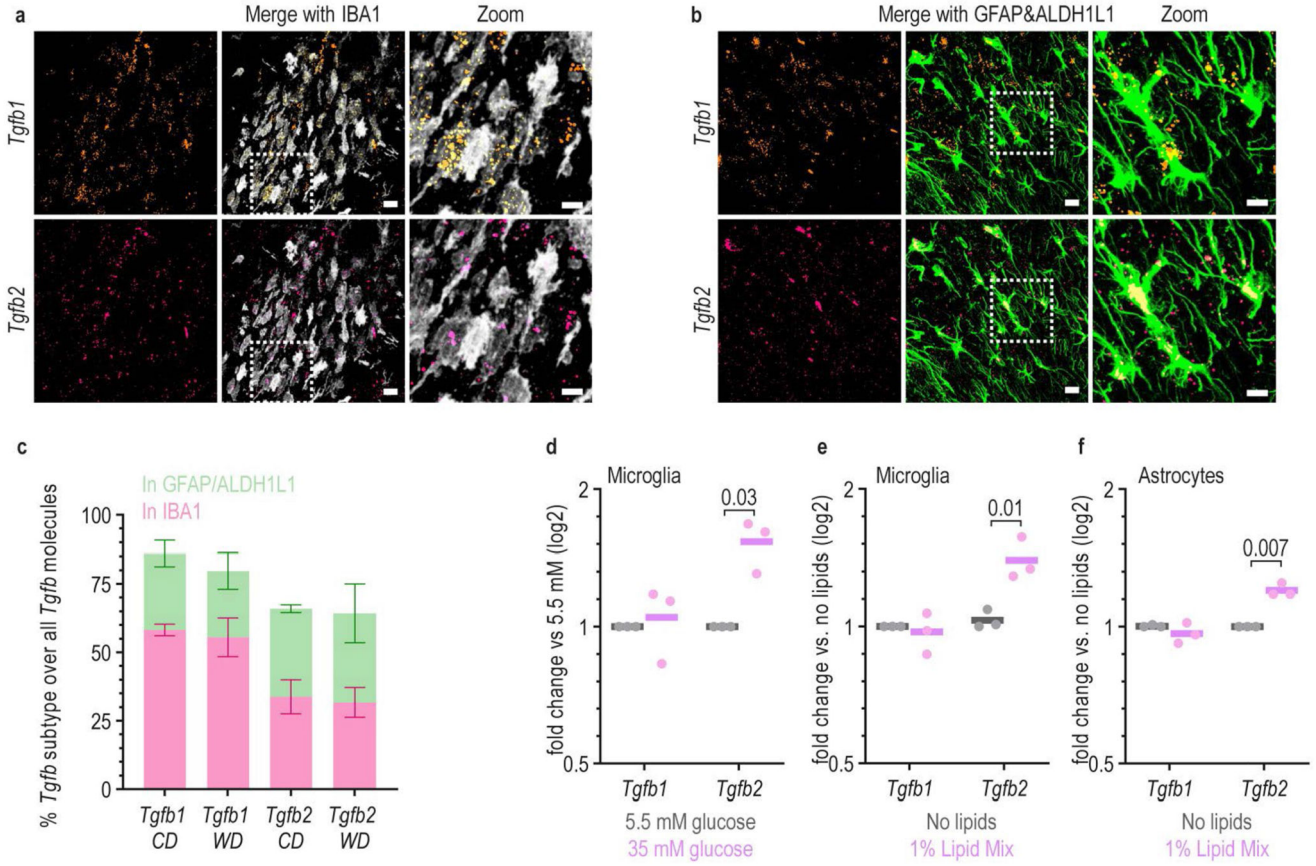


**Extended Data Fig.6. Distribution of TGFβ particles in the demyelinated lesion.**

**a,b**, Images of the fluorescent *in situ* hybridization of *Tgfb1* and *Tgfb2* in the demyelinated lesion at 2 dpi showing accumulation within IBA1$^+$ (**a**) cells or within GFAP&ALDH1L1$^+$ cells (**b**). Scale bar: 20μm in the overview, 10μm in the Zoom-in. **c**, Quantification of the percentage of *Tgfb1* and *Tgfb2* mRNA particles in IBA1$^+$ or in GFAP&ALDH1L1$^+$ cells over the total number of cells in a demyelinated lesion at 2 dpi. ((mean±SD, two-tailed




Europe PMC Funders Author Manuscripts

Welch's t-test). **d-f**, Expression change in *Tgfb1* and *Tgfb2* induced by high glucose concentrations in cultured primary microglia (**d**), high lipid concentrations in cultured primary microglia (**e**) and high lipid concentrations in cultured primary astrocytes (**f**) (two-tailed paired t-test). Solid lines in the graphs indicate the mean. P-values below 0.1 and n numbers are indicated in the figure. dpi: days post injection, CD: control diet, WD: Western diet.

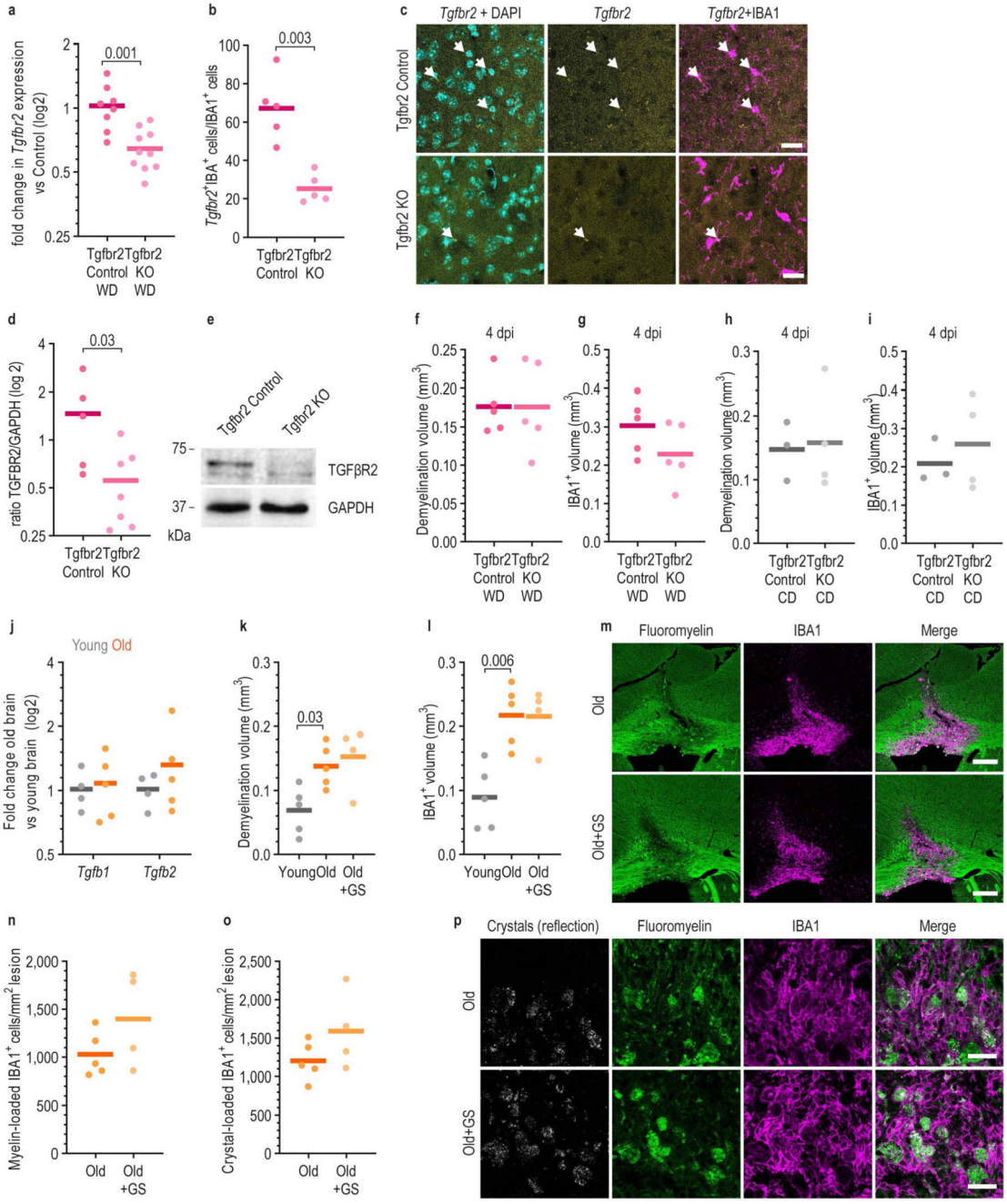


**Extended Data Fig.7. Blocking TGFβ signaling does not improve repair in old mice.**




Europe PMC Funders Author Manuscripts

Europe PMC Funders Author Manuscripts

**a**, Fold change in *Tgfbr2* expression in the demyelinated lesions of Tgfbr2 KO and control mice (two-tailed Welch's t-test). **b**, Quantification of the number of *Tgfbr2'* microglia in the unlesioned brains of Tgfbr2 KO and control mice (two-tailed Welch's t test). **c**, Images of the unlesioned brain of Tgfbr2 KO and control mice demonstrating the accumulation of *Tgfbr2* RNA particles within IBA1$^+$ microglia. Scale bar: 20μm. **d**, Quantification of the ratio of TGFβR2 signal over GAPDH signal in microglia isolated from Tgfbr2 KO and control mice (two-tailed t-test). **e**, Example images of the Western blots used for quantification of TGFβR2 levels of isolated microglia from Tgfbr2 KO and control mice. TGFβR2 levels were normalized to GAPDH. **f,g**, Quantification of the demyelination (**f**) and IBA1$^+$ (**g**) volume at 4 dpi in Tgfbr2 KO and control mice fed WD. **h,i**, Quantification of the demyelination (**h**) and IBA1$^+$ (**i**) volume at 4dpi in Tgfbr2 control and KO mice fed CD. **j**, Quantification of *Tgfbl* and *Tgfb2* expression in the unlesioned brain of young (3-months old) and old (12-months old) mice by RT-qPCR (two-tailed Welch's t-test). **k,l**, Quantification of demyelination k) and IBA1$^+$ (**l**) volume at 14 dpi in young, old and old +GS mice (one-way Brown-Forsythe and Welch ANOVA tests with multiple comparisons corrected by Dunnett T3 test). **m**, Images of corpus callosum lesions of old and old+GS mice at 14dpi. Scale bar: 200μm. **n,o**, Quantification of the number of myelin- (**n**) and crystal- (**o**) loaded IBA1$^+$ cells per mm$^2$ of lesion (two-tailed Welch's t-test). **p**, Images of the demyelinated lesion in the corpus callosum at 14dpi exemplifying myelin- and crystal-loaded IBA1$^+$ cells in old and old+GS mice. Scale bar: 20μm. N numbers are indicated in the figure; each dot represents one mouse. Solid lines in the graphs indicate the mean. CD: control diet, WD: Western diet GS: Galunisertib, dpi: days post injection.

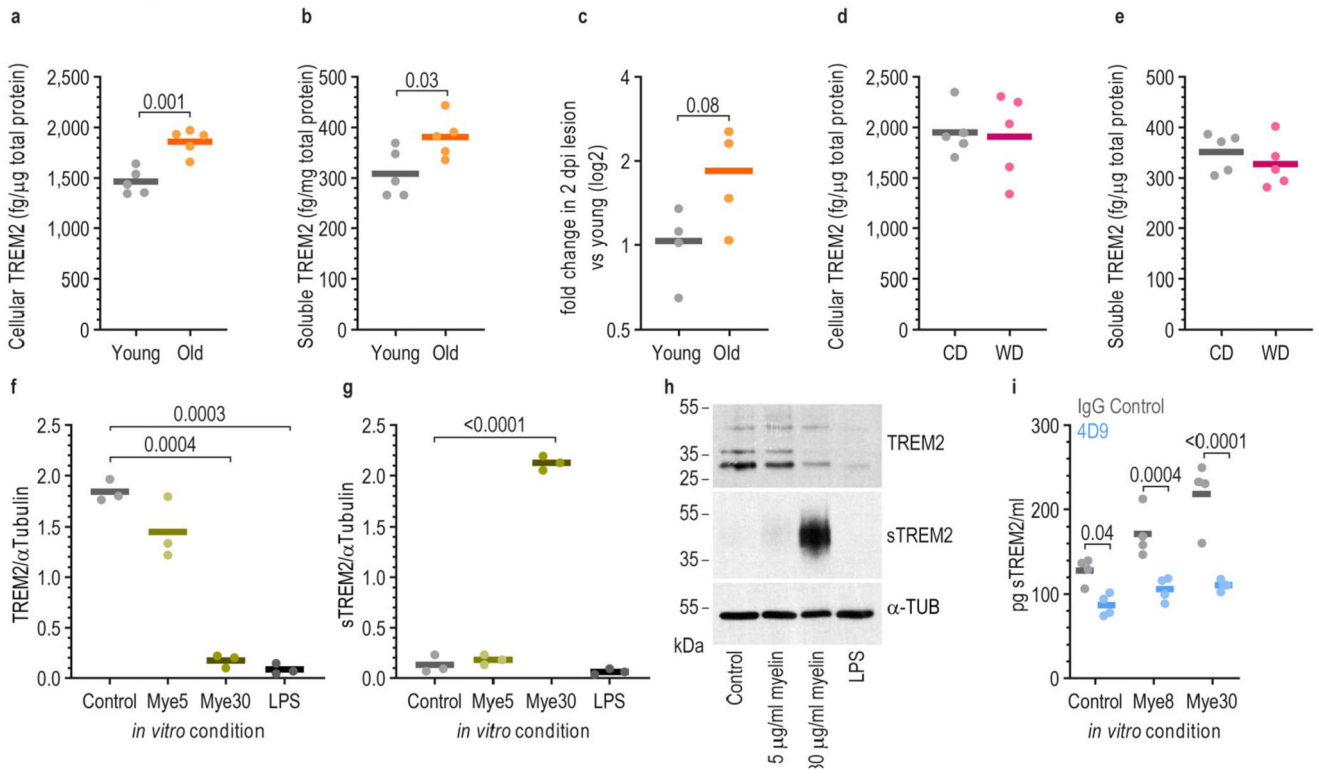

Europe PMC Funders Author Manuscripts

**Extended Data Fig.8. 4D9 treatment prevents myelin-induced TREM2 shedding.**

**a,d**, Quantification using ELISA of cellular TREM2 in the unlesioned brain of old (12-months old) and young (3-months old) mice (**a**) and of CD- and WD-fed mice (**d**) (two-tailed Welch's t-test). **b,e**, Quantification using ELISA of soluble TREM2 in the unlesioned brain old and young mice (**b**) and of CD- and WD-fed mice (**e**) (two-tailed Welch's t-test). **c**, Change in expression of *Trem2* in the demyelinated lesions of old mice at 2 dpi when compared to young mice (two-tailed Welch's t-test). **f,g**, Quantification of the band density in Western blots of TREM2-labelled (**f**) and sTREM2-labelled (**g**) bands normalized by the density of the bands labelled by α-TUBULIN (α-TUB). Microglia were treated with myelin for 24 hours (one-way Brown-Forsythe and Welch ANOVA tests with multiple comparisons corrected by Dunnett T3 test). **h**, Example images of the Western blots used for quantification of TREM2 and sTREM2 densities. Molecular weight ladders are indicated on the left side. **i**, Quantification by ELISA of the amounts of sTREM2 found in the media in different conditions. Microglia were treated with 20μg/mL of 4D9 antibody or IgG isotype control for 16hours, followed by 24hours of myelin treatment (two-tailed Welch's t-test). P-values and n numbers are indicated in the figure. Solid lines in the graphs indicate the mean. dpi: days post injection, CD: control diet, WD: Western diet, sTREM2: soluble TREM2, Mye5: 5μg/mL myelin treatment, Mye8: 8μg/mL myelin treatment, Mye30: 30μg/mL myelin treatment, 4D9: TREM2 enhancing antibody.

## Supplementary Material

Refer to Web version on PubMed Central for supplementary material.

## Acknowledgements

The work was supported by grants from the German Research Foundation (SPP2191, TRR128-2, TRR 274 Project ID 408885537, Koselleck Project HA1737/16-1, SyNergy Excellence Cluster, EXC2145, Projekt ID390857198), the Human Frontier Science Program (HFSP), the ERC (Consolidator Grant to M.S.), and the Dr. Miriam and Sheldon G. Adelson Medical Research Foundation. M.B.Q. was supported by a Boehringer Ingelheim Fonds PhD fellowship. We would like to thank A. Rhomberg, G. Kislinger, A. Kerksiek and K. Karg for their technical assistance.

## Data availability

The data that support the findings of this study are available from the corresponding author upon request. Source data for the lipidomics analyses and uncropped images of western blots are provided. Source data are provided with this paper.

## Code availability

The script used for lesion volume analysis can be found at: https://github.com/lenkavaculciakova/lesion_volume

## References

1. Hotamisligil GS. Inflammation, metaflammation and immunometabolic disorders. Nature. 2017; 542:177–185. [PubMed: 28179656]
2. Hansson GK, Hermansson A. The immune system in atherosclerosis. Nat Immunol. 2011; 12:204–212. [PubMed: 21321594]

Europe PMC Funders Author Manuscripts


3. Chawla A, Nguyen KD, Goh YP. Macrophage-mediated inflammation in metabolic disease. Nat Rev Immunol. 2011; 11:738–749. [PubMed: 21984069]
4. Lloyd AF, Miron VE. The pro-remyelination properties of microglia in the central nervous system. Nat Rev Neurol. 2019; doi: 10.1038/s41582-019-0184-2
5. Franklin RJM, Ffrench-Constant C. Regenerating CNS myelin—from mechanisms to experimental medicines. Nat Rev Neurosci. 2017; 18:753–769. [PubMed: 29142295]
6. Plemel JR, Liu WQ, Yong VW. Remyelination therapies: a new direction and challenge in multiple sclerosis. Nat Rev Drug Discov. 2017; 16:617–634. [PubMed: 28685761]
7. Lampron A, et al. Inefficient clearance of myelin debris by microglia impairs remyelinating processes. J Exp Med. 2015; 212:481–495. [PubMed: 25779633]
8. Kotter MR, Li WW, Zhao C, Franklin RJ. Myelin impairs CNS remyelination by inhibiting oligodendrocyte precursor cell differentiation. J Neurosci. 2006; 26:328–332. [PubMed: 16399703]
9. Prinz M, Jung S, Priller J. Microglia biology: one century of evolving concepts. Cell. 2019; 179:292–311. [PubMed: 31585077]
10. Stadelmann C, Timmler S, Barrantes-Freer A, Simons M. Myelin in the Central Nervous System: Structure, Function, and Pathology. Physiol Rev. 2019; 99:1381–1431. [PubMed: 31066630]
11. Miron VE, et al. M2 microglia and macrophages drive oligodendrocyte differentiation during CNS remyelination. Nat Neurosci. 2013; 16:1211–1218. [PubMed: 23872599]
12. Dombrowski Y, et al. Regulatory T cells promote myelin regeneration in the central nervous system. Nat Neurosci. 2017; 20:674–680. [PubMed: 28288125]
13. Yeung MSY, et al. Dynamics of oligodendrocyte generation in multiple sclerosis. Nature. 2019; 566:538–542. [PubMed: 30675058]
14. Jakel S, et al. Altered human oligodendrocyte heterogeneity in multiple sclerosis. Nature. 2019; doi: 10.1038/s41586-019-0903-2
15. Kuhlmann T, et al. Differentiation block of oligodendroglial progenitor cells as a cause for remyelination failure in chronic multiple sclerosis. Brain. 2008; 131:1749–1758. [PubMed: 18515322]
16. Patrikios P, et al. Remyelination is extensive in a subset of multiple sclerosis patients. Brain. 2006; 129:3165–3172. [PubMed: 16921173]
17. Chang A, Tourtellotte WW, Rudick R, Trapp BD. Premyelinating oligodendrocytes in chronic lesions of multiple sclerosis. N Engl J Med. 2002; 346:165–173. [PubMed: 11796850]
18. Reich DS, Lucchinetti CF, Calabresi PA. Multiple sclerosis. N Engl J Med. 2018; 378:169–180. [PubMed: 29320652]
19. Baecher-Allan C, Kaskow BJ, Weiner HL. Multiple sclerosis: mechanisms and immunotherapy. Neuron. 2018; 97:742–768. [PubMed: 29470968]
20. Neumann B, et al. Metformin restores CNS remyelination capacity by rejuvenating aged stem cells. Cell Stem Cell. 2019; 25:473–485. [PubMed: 31585093]
21. Cantuti-Castelvetri L, et al. Defective cholesterol clearance limits remyelination in the aged central nervous system. Science. 2018; doi: 10.1126/science.aan4183
22. Ruckh JM, et al. Rejuvenation of regeneration in the aging central nervous system. Cell Stem Cell. 2012; 10:96–103. [PubMed: 22226359]
23. Shen S, et al. Age-dependent epigenetic control of differentiation inhibitors is critical for remyelination efficiency. Nat Neurosci. 2008; 11:1024–1034. [PubMed: 19160500]
24. Sim FJ, Zhao C, Penderis J, Franklin RJ. The age-related decrease in CNS remyelination efficiency is attributable to an impairment of both oligodendrocyte progenitor recruitment and differentiation. J Neurosci. 2002; 22:2451–2459. [PubMed: 11923409]
25. Gianfrancesco MA, Barcellos LF. Obesity and multiple sclerosis susceptibility: a review. J Neurol Neuromedicine. 2016; 1:1–5.
26. Munger KL, Chitnis T, Ascherio A. Body size and risk of MS in two cohorts of US women. Neurology. 2009; 73:1543–1550. [PubMed: 19901245]
27. Dalby MJ, Ross AW, Walker AW, Morgan PJ. Dietary uncoupling of gut microbiota and energy harvesting from obesity and glucose tolerance in mice. Cell Rep. 2017; 21:1521–1533. [PubMed: 29117558]

28. Jeffery ND, Blakemore WF. Remyelination of mouse spinal cord axons demyelinated by local injection of lysolecithin. J Neurocytol. 1995; 24:775–781. [PubMed: 8586997]
29. Plemel JR, et al. Microglia response following acute demyelination is heterogeneous and limits infiltrating macrophage dispersion. Sci Adv. 2020; 6
30. Lloyd AF, et al. Central nervous system regeneration is driven by microglia necroptosis and repopulation. Nat Neurosci. 2019; 22:1046–1052. [PubMed: 31182869]
31. Zhang Y, et al. Positional cloning of the mouse obese gene and its human homologue. Nature. 1994; 372:425–432. [PubMed: 7984236]
32. Evans RM, Mangelsdorf DJ. Nuclear receptors, RXR, and the Big Bang. Cell. 2014; 157:255–266. [PubMed: 24679540]
33. Huang JK, et al. Retinoid X receptor gamma signaling accelerates CNS remyelination. Nat Neurosci. 2011; 14:45–53. [PubMed: 21131950]
34. Cunha MI, et al. Pro-inflammatory activation following demyelination is required for myelin clearance and oligodendrogenesis. J Exp Med. 2020; 217
35. Bogie JFJ, et al. Stearoyl-CoA desaturase-1 impairs the reparative properties of macrophages and microglia in the brain. J Exp Med. 2020; 217
36. Fielding CJ, Fielding PE. Molecular physiology of reverse cholesterol transport. J Lipid Res. 1995; 36:211–228. [PubMed: 7751809]
37. Bogie JF, et al. Myelin-derived lipids modulate macrophage activity by liver X receptor activation. PLoS ONE. 2012; 7
38. Spann NJ, et al. Regulated accumulation of desmosterol integrates macrophage lipid metabolism and inflammatory responses. Cell. 2012; 151:138–152. [PubMed: 23021221]
39. Schroepfer GJ Jr. Oxysterols: modulators of cholesterol metabolism and other processes. Physiol Rev. 2000; 80:361–554. [PubMed: 10617772]
40. Yan J, et al. Obesity- and aging-induced excess of central transforming growth factor-beta potentiates diabetic development via an RNA stress response. Nat Med. 2014; 20:1001–1008. [PubMed: 25086906]
41. Samad F, Yamamoto K, Pandey M, Loskutoff DJ. Elevated expression of transforming growth factor-beta in adipose tissue from obese mice. Mol Med. 1997; 3:37–48. [PubMed: 9132278]
42. Butovsky O, et al. Identification of a unique TGF-β-dependent molecular and functional signature in microglia. Nat Neurosci. 2014; 17:131–143. [PubMed: 24316888]
43. Wrana JL, Attisano L, Wieser R, Ventura F, Massague J. Mechanism of activation of the TGF-βreceptor. Nature. 1994; 370:341–347. [PubMed: 8047140]
44. Zoller T, et al. Silencing of TGFβsignalling in microglia results in impaired homeostasis. Nat Commun. 2018; 9:4011. [PubMed: 30275444]
45. Seystahl K, Wick W, Weller M. Therapeutic options in recurrent glioblastoma-an update. Crit Rev Oncol Hematol. 2016; 99:389–408. [PubMed: 26830009]
46. Song WM, Colonna M. The identity and function of microglia in neurodegeneration. Nat Immunol. 2018; 19:1048–1058. [PubMed: 30250185]
47. Cignarella F, et al. TREM2 activation on microglia promotes myelin debris clearance and remyelination in a model of multiple sclerosis. Acta Neuropathol. 2020; doi: 10.1007/s00401-020-02193-z
48. Deczkowska A, Amit I, Schwartz M. Microglial immune checkpoint mechanisms. Nat Neurosci. 2018; 21:779–786. [PubMed: 29735982]
49. Jaitin DA, et al. Lipid-associated macrophages control metabolic homeostasis in a Trem2-dependent manner. Cell. 2019; 178:686–698. [PubMed: 31257031]
50. Nugent AA, et al. TREM2 regulates microglial cholesterol metabolism upon chronic phagocytic challenge. Neuron. 2019; doi: 10.1016/j.neuron.2019.12.007
51. Keren-Shaul H, et al. A unique microglia type associated with restricting development of Alzheimer's disease. Cell. 2017; 169:1276–1290. [PubMed: 28602351]
52. Kleinberger G, et al. TREM2 mutations implicated in neurodegeneration impair cell surface transport and phagocytosis. Sci Transl Med. 2014; 6


Europe PMC Funders Author Manuscripts

53. Wunderlich P, et al. Sequential proteolytic processing of the triggering receptor expressed on myeloid cells-2 (TREM2) protein by ectodomain shedding and gamma-secretase-dependent intramembranous cleavage. J Biol Chem. 2013; 288:33027–33036. [PubMed: 24078628]
54. Schlepckow K, et al. Enhancing protective microglial activities with a dual function TREM2 antibody to the stalk region. EMBO Mol Med. 2020; 12
55. Kalin S, et al. Hypothalamic innate immune reaction in obesity. Nat Rev Endocrinol. 2015; 11:339–351. [PubMed: 25824676]
56. Madore C, Yin Z, Leibowitz J, Butovsky O. Microglia, lifestyle stress, and neurodegeneration. Immunity. 2020; doi: 10.1016/j.immuni.2019.12.003
57. Guillemot-Legris O, Muccioli GG. Obesity-induced neuroinflammation: beyond the hypothalamus. Trends Neurosci. 2017; 40:237–253. [PubMed: 28318543]
58. Prinz M, Priller J. Microglia and brain macrophages in the molecular age: from origin to neuropsychiatric disease. Nat Rev Neurosci. 2014; 15:300–312. [PubMed: 24713688]
59. Deczkowska A, et al. Disease-associated microglia: a universal immune sensor of neurodegeneration. Cell. 2018; 173:1073–1081. [PubMed: 29775591]
60. Krasemann S, et al. The TREM2-APOE pathway drives the transcriptional phenotype of dysfunctional microglia in neurodegenerative diseases. Immunity. 2017; 47:566–581. [PubMed: 28930663]
61. Grajchen E, Hendriks JJA, Bogie JFJ. The physiology of foamy phagocytes in multiple sclerosis. Acta Neuropathol Commun. 2018; 6:124. [PubMed: 30454040]
62. Endo F, et al. Astrocyte-derived TGF-β1 accelerates disease progression in ALS mice by interfering with the neuroprotective functions of microglia and T cells. Cell Rep. 2015; 11:592–604. [PubMed: 25892237]
63. Baror R, et al. Transforming growth factor-beta renders ageing microglia inhibitory to oligodendrocyte generation by CNS progenitors. Glia. 2019; 67:1374–1384. [PubMed: 30861188]
64. Xu J, et al. TGF-βin mice ameliorates experimental autoimmune encephalomyelitis in regulating NK cell activity. Cell Transplant. 2019; 28:1155–1160. [PubMed: 31137960]
65. Hamaguchi M, et al. Circulating transforming growth factor-β1 facilitates remyelination in the adult central nervous system. eLife. 2019; 8
66. Berghoff SA, et al. Dietary cholesterol promotes repair of demyelinated lesions in the adult brain. Nat Commun. 2017; 8
67. Yoon H, et al. Interplay between exercise and dietary fat modulates myelinogenesis in the central nervous system. Biochim Biophys Acta. 2016; 1862:545–555. [PubMed: 26826016]
68. Najm FJ, et al. Drug-based modulation of endogenous stem cells promotes functional remyelination in vivo. Nature. 2015; 522:216–220. [PubMed: 25896324]
69. Mei F, et al. Micropillar arrays as a high-throughput screening platform for therapeutics in multiple sclerosis. Nat Med. 2014; 20:954–960. [PubMed: 24997607]
70. Deshmukh VA, et al. A regenerative approach to the treatment of multiple sclerosis. Nature. 2013; 502:327–332. [PubMed: 24107995]
71. Wang S, et al. Anti-human TREM2 induces microglia proliferation and reduces pathology in an Alzheimer's disease model. J Exp Med. 2020; 217
72. Berner DK, et al. Meprin beta cleaves TREM2 and controls its phagocytic activity on macrophages. FASEB J. 2020; 34:6675–6687. [PubMed: 32237095]
73. Sosic-Jurjevic B, et al. The isoflavones genistein and daidzein increase hepatic concentration of thyroid hormones and affect cholesterol metabolism in middle-aged male rats. J Steroid Biochem Mol Biol. 2019; 190:1–10. [PubMed: 30885834]
74. Thelen KM, et al. Brain cholesterol synthesis in mice is affected by high dose of simvastatin but not of pravastatin. J Pharmacol Exp Ther. 2006; 316:1146–1152. [PubMed: 16282522]
75. Sampaio JL, et al. Membrane lipidome of an epithelial cell line. Proc Natl Acad Sci USA. 2011; 108:1903–1907. [PubMed: 21245337]
76. Ejsing CS, et al. Global analysis of the yeast lipidome by quantitative shotgun mass spectrometry. Proc Natl Acad Sci USA. 2009; 106:2136–2141. [PubMed: 19174513]

77. Herzog R, et al. A novel informatics concept for high-throughput shotgun lipidomics based on the molecular fragmentation query language. Genome Biol. 2011; 12:R8. [PubMed: 21247462]
78. Fitzner D, et al. Cell-type- and brain-region-resolved mouse brain lipidome. Cell Rep. 2020; 32
79. Duewell P, et al. NLRP3 inflammasomes are required for atherogenesis and activated by cholesterol crystals. Nature. 2010; 464:1357–1361. [PubMed: 20428172]
80. Schindelin J, et al. Fiji: an open-source platform for biological-image analysis. Nat Methods. 2012; 9:676–682. [PubMed: 22743772]



Europe PMC Funders Author Manuscripts

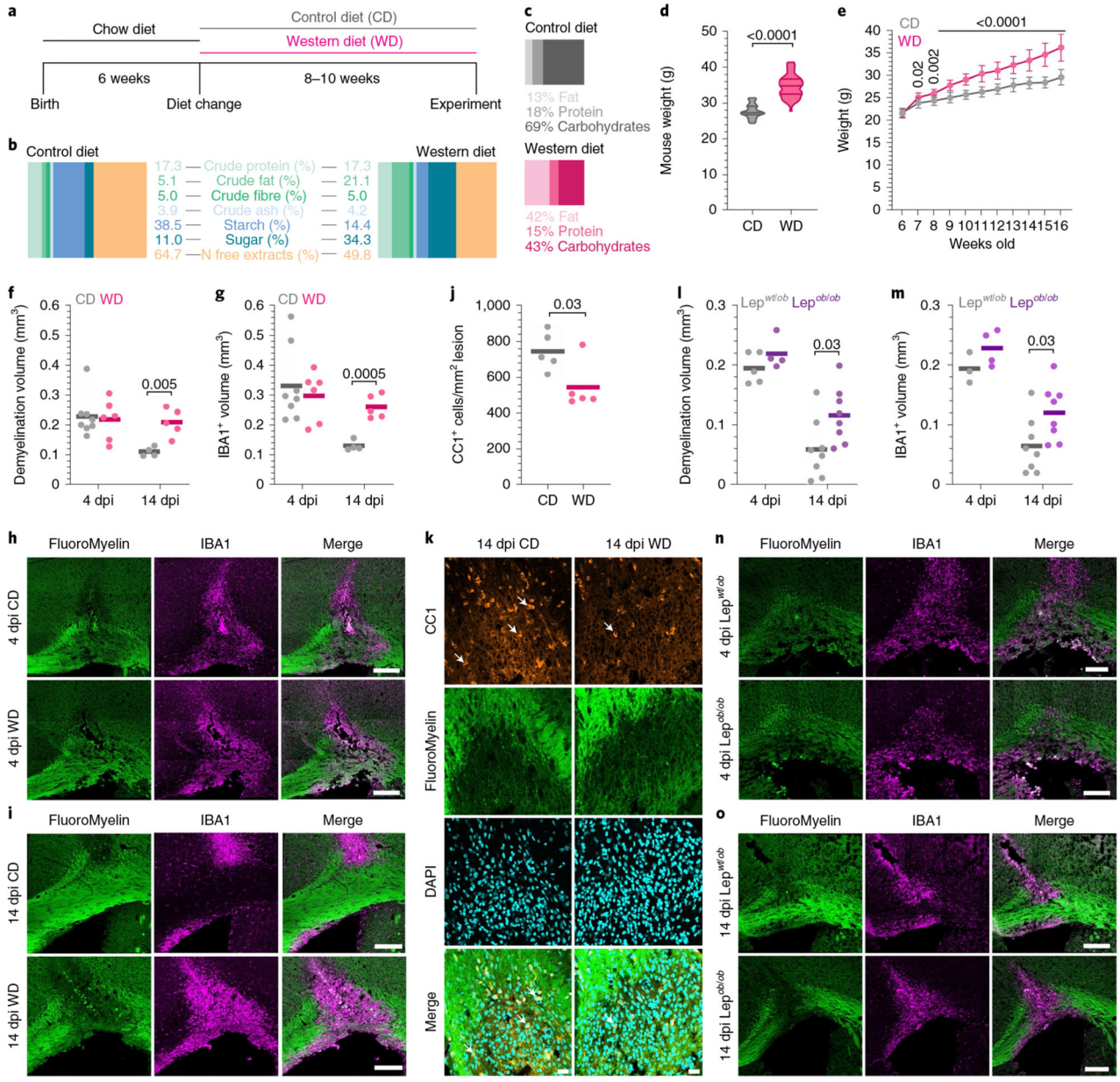


**Fig. 1. WD impairs lesion recovery after demyelinating injury.**

**a**, Schematic representation of the diet and timeline. **b**, Illustration showing the percentage of crude nutrients in CD and WD. **c**, Illustration of the percentage of metabolizable energy contained in fat, proteins and carbohydrates. **d**, Violin plot of the body weight of mice fed WD or CD for 10 weeks. Solid lines indicate the 25%, 50% and 75% quartiles. For CD, $n$ = 52; for WD, $n$ = 54 (two-tailed Welch's $t$-test). **e**, Body weight increase over time either under the CD or WD ($n$ = 10 for both groups, data represent mean±s.d., two-tailed Welch's $t$-test). **f**,**g**, Demyelination (**f**) and IBA1 $^{+}$ (**g**) volume at 4 and 14dpi in CD- and WD-fed mice. Solid lines indicate the mean (two-tailed Welch's $t$-test). **h**,**i**, Images of corpus




Europe PMC Funders Author Manuscripts

callosum lesions in CD- and WD-fed mice at 4 (**h**) and 14 (**i**) dpi. Scale bar, 200 μm. **j**, Quantification of the number of $CC1^+$ cells per $mm^2$ of lesion. Solid lines indicate the mean (two-tailed Welch's *t*-test). **k**, Images of the demyelinated lesions in the corpus callosum at 14 dpi exemplifying the numbers of $CC1^+$ cells at the demyelination-remyelination edge. White arrows indicate $CC1^+$ cells. Scale bar, 20 μm. **l**,**m**, Demyelination (**l**) and $IBA1^+$ (**m**) volume at 4 and 14dpi in $lep^{wt/ob}$ and $lep^{ob/ob}$ mice. Solid lines indicate the mean (two-tailed Welch's *t*-test). **n**,**o**, Images of corpus callosum lesions in $lep^{wt/ob}$ and $lep^{ob/lb}$mice at 4 (**n**) and 14 (**o**) dpi. Scale bar, 200μm. *P* values below 0.1 and *n* numbers are indicated in the figure; each dot represents one mouse.

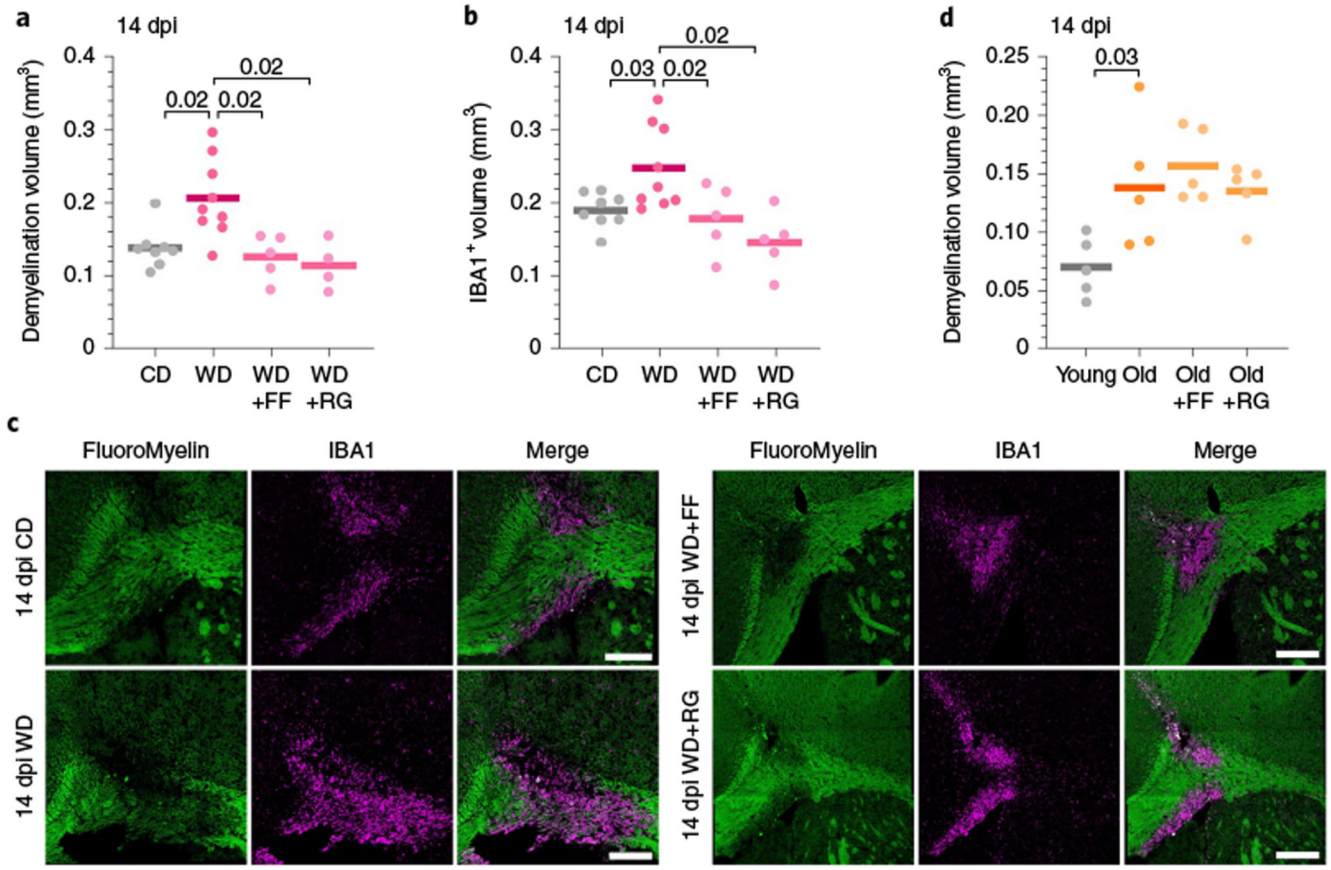


**Fig. 2. Correcting metabolic alterations induced by WD improves lesion recovery after demyelination.**

**a,b**, Quantification of demyelination (**a**) and IBA1$^+$ (**b**) volume at 14dpi in CD-, WD-, WD +FF- and WD+RG-fed mice (one-way Brown-Forsythe and Welch ANOVA tests with multiple comparisons corrected by Dunnett T3 test). **c**, Images of corpus callosum lesions of all treatment groups at 14 dpi. Scale bar, 200 μm. **d**, Quantification of the demyelination volume at 14 dpi in old, old+FF and old+RG mice. We observed no differences between treatment groups (one-way Brown-Forsythe and Welch ANOVA tests with multiple comparisons corrected by Dunnett T3 test). *P*-values below 0.1 and *n* values are indicated in the figure; each dot represents one mouse. Solid lines in the graphs indicate the mean. WD +FF, WD supplemented with FF; WF+RG, WD supplemented with RG; Old+FF, old mice fed FF-containing chow; Old+RG, old mice fed RG-containing chow.




Europe PMC Funders Author Manuscripts

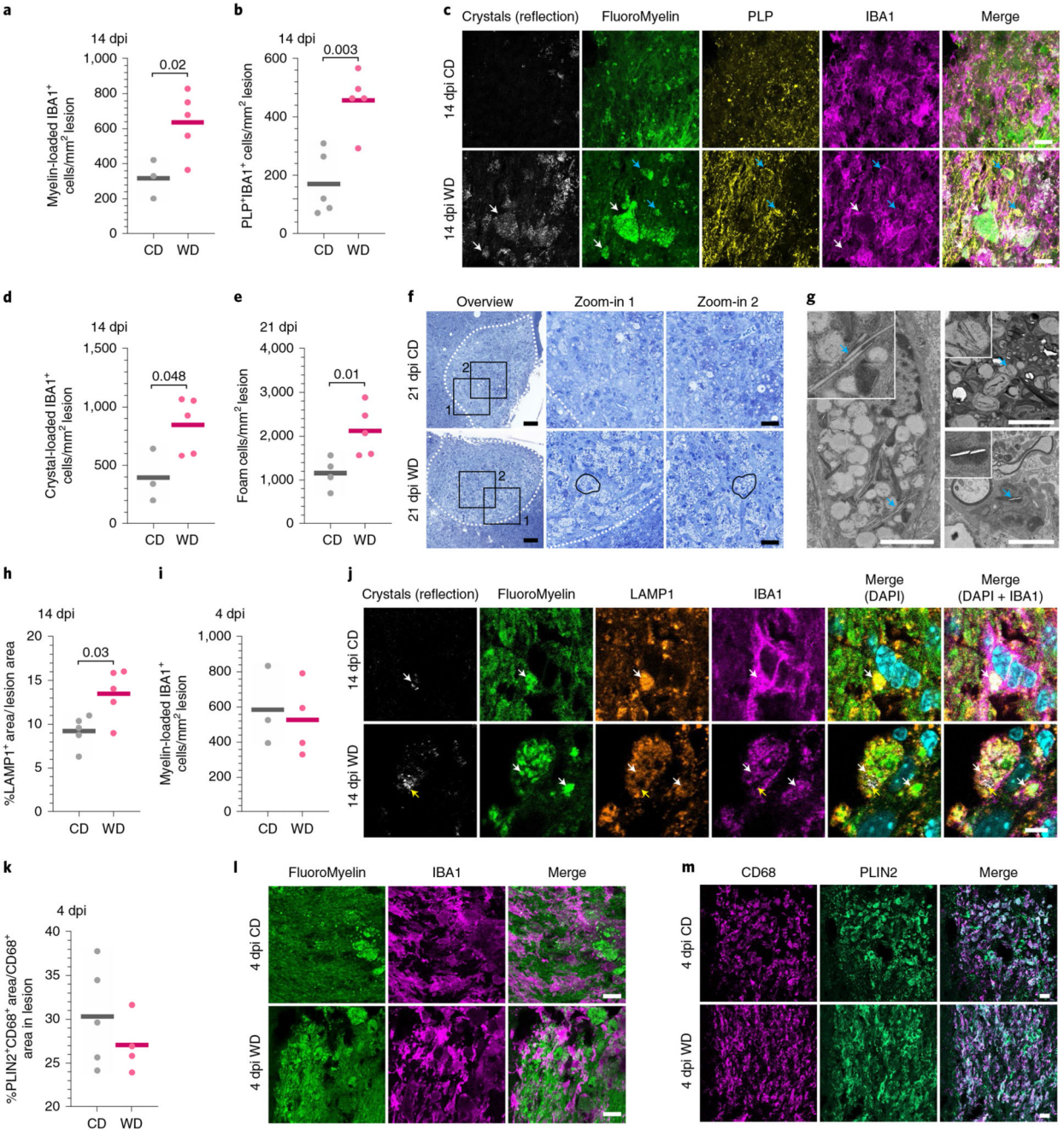


**Fig. 3. Demyelinated lesions of WD-fed mice accumulate myelin- and crystal-loaded phagocytes.**

**a**,**b**,**d**, Quantification of the number of myelin- (**a**), PLP- (**b**) and crystal-loaded (**d**) IBA1$^+$ cells per mm$^2$ of lesion at 14dpi (two-tailed Welch's *t*-test). **c**, Images of the demyelinated lesions in the corpus callosum at 14dpi showing myelin- and crystal-loaded IBA1$^+$ cells in CD- and WD-fed mice. White arrows indicate myelin- and crystal-loaded IBA1$^+$ cells. Blue arrows indicate myelin-loaded IBA1$^+$ cells. Scale bar, 20μm. **e**, Quantification of foam cells per mm$^2$ of lesion at 21 dpi (two-tailed Welch's *t*-test). **f**, Images of demyelinated lesions in the spinal cord of CD- and WD-fed mice at 21 dpi demonstrating foam-cell accumulation.

Europe PMC Funders Author Manuscripts

Examples of foam cells are circled with a solid black line. The demyelinated area is indicated with a dashed line. The zoom-in regions are indicated in the overview as squares. Scale bar, overview 50 μm, zoom-in 20μm. **g**, Electron microscopy images demonstrating crystal accumulation in the cytoplasm (left), lipid droplets (top right) and lysosomes (bottom right). Blue arrows indicate crystals shown in the magnification on the top left corner of each image. Scale bar, 2.5μm. **h**, Quantification of the percentage of lesion area occupied by $LAMP1^+$ signal in the 14dpi lesion (two-tailed Welch's *t*-test). **j**, Images demonstrating accumulation of myelin debris in $LAMP1^+$ lysosomes of $IBA1^+$ cells in demyelinated lesions at 14dpi. White arrows point to myelin-debris accumulation within $LAMP1^+$ organelles of $IBA1^+$ cells. Yellow arrows indicate crystal accumulation within an $IBA1^+$ cell. Scale bar, 5μm. **i**,**k**, Quantification of myelin-loaded $IBA1^+$ cells (**i**) and the percentage of $PLIN^+CD68^+$ signal (**k**) in demyelinated lesions at 4dpi. **l**, Images of demyelinated lesions in the corpus callosum at 4dpi demonstrating myelin accumulation within $IBA1^+$ phagocytes. Scale bar, 20μm. **m**, Images of demyelinated lesions at 4 dpi demonstrating $PLIN^+$ signal within $CD68^+$ phagocytes. Scale bar, 20μm. *P*-values below 0.1 and *n* numbers are indicated in the figure; each dot represents one mouse. Solid lines in the graphs indicate the mean.

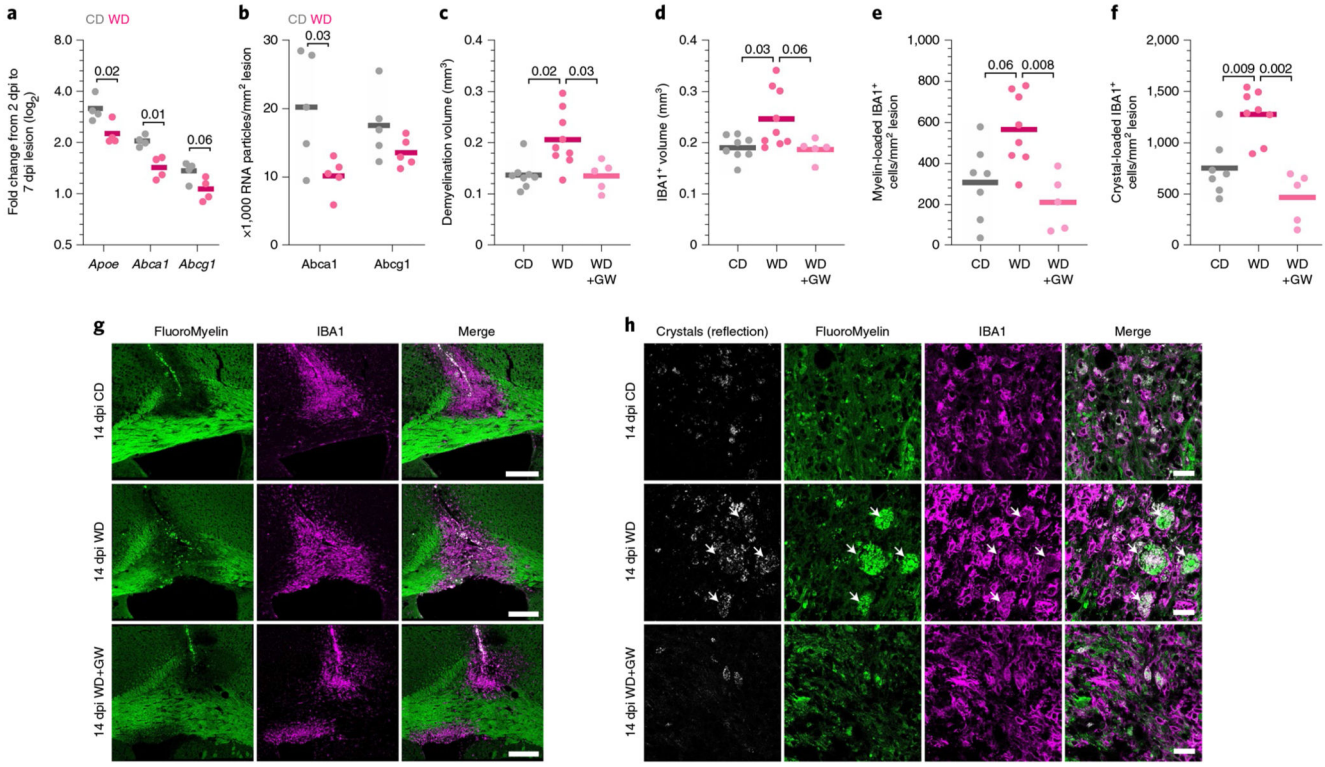


**Fig. 4. The LXR pathway is insufficiently activated in WD-fed mice.**

**a**, Quantification of the increase in mRNA expression of *Apoe, Abca1* and *Abcg1* from 2 to 7 dpi lesions from CD- and WD-fed mice by RT-qPCR (two-tailed Welch's *t*-test). **b**, Quantification of the numbers of *Abca1* and *Abcg1* RNA particles visualized by in situ RNA hybridization within the demyelinated lesions at 14dpi in CD- and WD-fed mice (two-tailed Welch's *t*-test). **c,d**, Quantification of demyelination (**c**) and IBA1 $^{+}$ (**d**) volume at 14dpi in CD-, WD- and WD+GW-fed mice (one-way Brown-Forsythe and Welch ANOVA tests with multiple comparisons corrected by Dunnett T3 test). The reference groups (CD and WD) are from Fig. 2a,b. **e**,**f**, Quantification of the number of myelin- (**e**) and crystal-loaded (**f**) IBA1$^{+}$ cells per mm$^{2}$ of lesion (one-way Brown-Forsythe and Welch ANOVA tests with multiple comparisons corrected by Dunnett T3 test). **g**, Images of corpus callosum lesions of all groups at 14 dpi. Scale bars, 200 μm. **h**, Images of the demyelinated lesion in the corpus callosum at 14 dpi, exemplifying myelin- and crystal-loaded IBA1$^{+}$ cells in all treatment groups. White arrows indicate myelin- and crystal-loaded IBA1$^{+}$ phagocytes. Scale bars, 20μm. *P*-values below 0.1 and *n* numbers are indicated in the figure; each dot represents one mouse. Solid lines in the graphs indicate the mean. WD+GW, WD supplemented with GW3965.




Europe PMC Funders Author Manuscripts

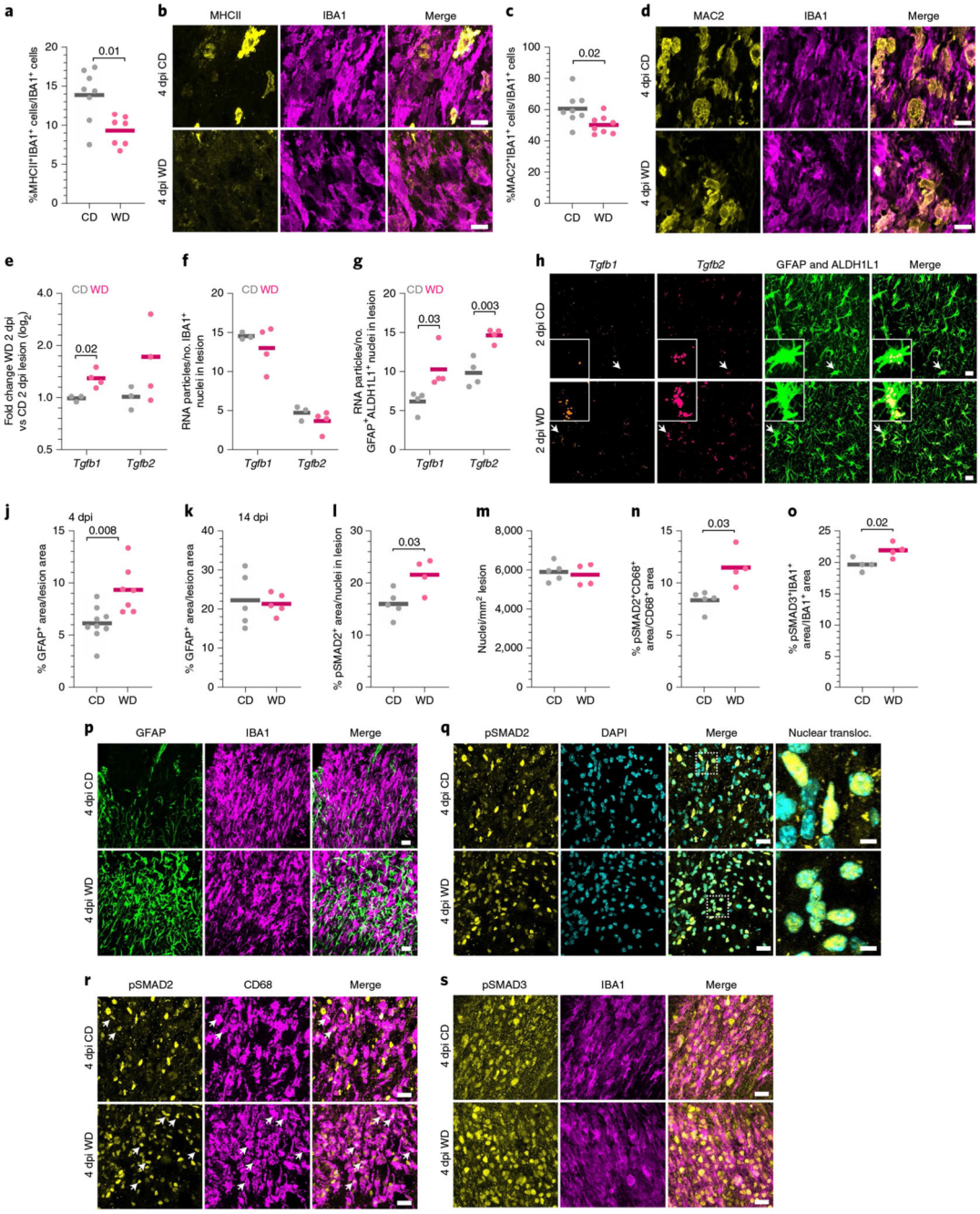


**Fig. 5. Impaired microglia activation correlates with increased TGFβ signalling in the brain after WD feeding.**

**a**,**c**, Quantification of the percentage of MHCII$^+$IBA1$^+$ cells (**a**) and MAC2$^+$IBA1$^+$ cells (**c**) over IBA1$^+$ cells in the demyelinated lesion at 4dpi (two-tailed Welch's *t*-test). **b**,**d**, Images of MHCII$^+$IBA1$^+$ (**b**) and MAC2$^+$IBA1$^+$ (**d**) cells in the demyelinated lesions at 4dpi. Scale bar, 10 μm. **e**, Quantification of *Tgfbl* and *Tgfb2* expression in the 2 dpi lesion by RT- qPCR (two-tailed Welch's t-test). **f**,**g**, Quantification of *Tgfbl* and *Tgfb2* RNA particles visualized by RNA in situ hybridization within IBA1$^+$ cells (**f**) or within GFAP$^+$ALDH1L1$^+$ cells (**g**)




Europe PMC Funders Author Manuscripts

Europe PMC Funders Author Manuscripts

(two-tailed Welch's *t*-test). **h**, Images of the demyelinated lesions at 2 dpi demonstrating the accumulation of *Tgfbl* and *Tgfb2* transcripts in $GFAP^+ALDH1L1^+$ cells. Scale bar, 20 μm. White arrows indicate the cell shown in the zoom-in panel. **j**,**k**, Quantification of lesion area covered by $GFAP^+$ signal at 4dpi (**j**) and 14dpi (**k**) (two-tailed Welch's *t*-test). **l**,**m**, Quantification of the lesion area covered by pSMAD2 over the number of nuclei (**l**) and the number of nuclei per $mm^2$ of lesion (**m**) in the demyelinated lesions at 4dpi (two-tailed Welch's *t*-test). **n**,**o**, Quantification of the $pSMAD2^+$ signal within $CD68^+$ area (**n**) and of the $pSMAD3^+$ signal within $IBA1^+$ area (**o**) in the demyelinated lesions at 4dpi (two-tailed Welch's *t*-test). **p**, Images of the demyelinated lesion at 4 dpi demonstrating the accumulation of $GFAP^+$ signal. Scale bar, 20 μm. **q**, Images of demyelinated lesions at 4 dpi showing pSMAD2 and DAPI staining and nuclear translocation of pSMAD2. Scale bar, 20 μm in overview, 5μm in the images demonstrating nuclear translocation of pSMAD2. **r**, Images of the demyelinated lesion at 4dpi demonstrating pSMAD2 and CD68 staining. White arrows point to $CD68^+$ cells accumulating $pSMAD2^+$ signal within their nucleus. Scale bar, 20μm. **s**, Images of the demyelinated lesion at 4dpi demonstrating pSMAD3 and IBA1 staining. Scale bar, 20μm. Solid lines in the graphs indicate the mean. *P*-values below 0.1 and *n* numbers are indicated in the figure; each dot represents one mouse.

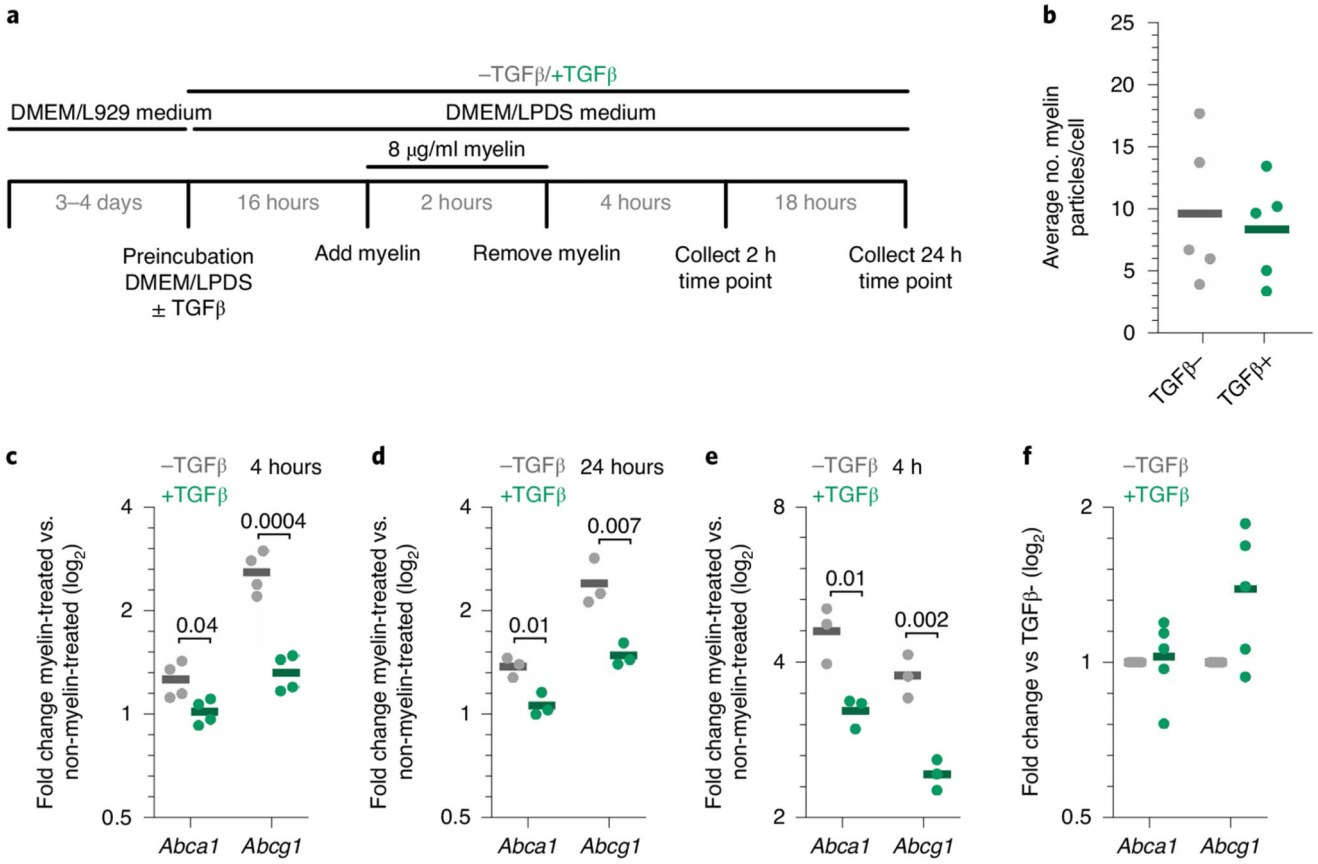


**Fig. 6. TGFβ blocks cholesterol efflux gene induction after myelin uptake.**

**a**, Schematic representation of the in vitro experimental approach to analyse induction of *Abca1* and *Abcg1* in microglia upon myelin treatment and TGFβ treatment. LPDS, lipoprotein-deficient serum; L929, L929 cell line conditioned media. **b**, Quantification of the average number of $PLP^+$ myelin particles within phagocytes after 2 hours of incubation with myelin in TGFβ-treated and control cells. **c**,**d**, Quantification of the increase in mRNA expression of *Abca1* and *Abcg1* 4hours (**c**) and 24hours (**d**) after myelin phagocytosis with or without TGFβ treatment in primary microglia (two-tailed Welch's *t*-test). **e**, Quantification of the increase in mRNA expression of *Abca1* and *Abcg1* 4hour after myelin phagocytosis with or without TGFβ treatment in BMDMs (two-tailed Welch's *t*-test). **f**, Quantification of the increase in mRNA expression o' *Abca1* and *Abcg1* induced by TGFβ in TGFβ-treated and control cells. No significant differences were observed (two-tailed Welch's *t*-test). Solid lines in th graphs indicate the mean. *P*-values below 0.1 and *n* numbers are indicated in the figure.




Europe PMC Funders Author Manuscripts

Europe PMC Funders Author Manuscripts

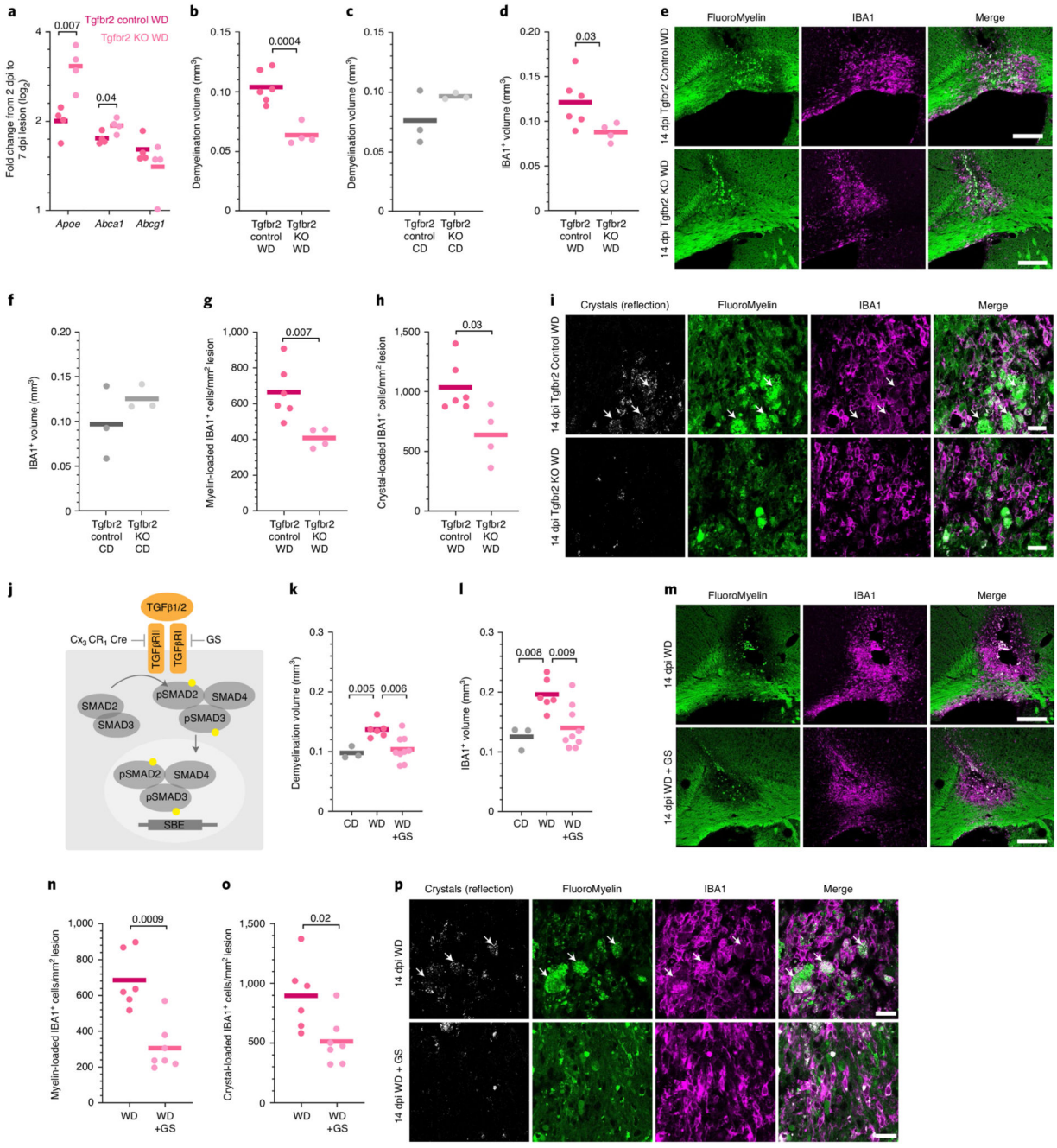


**Fig. 7. Blocking TGFβ signalling in microglia of WD-fed mice promotes recovery from demyelinating inj'ury.**

**a**, Quantification of the increase in mRNA expression of *Apoe, Abca1* and *Abcg1* from 2 to 7dpi lesions from *Cx3cr1*$^{creERT,wt}$*:Tgfbr2*$^{fl/f,}$ (Tgfbr2 KO) or *Cx3cr1*$^{wt,wt}$*:Tgfbr2*$^{fl/fl}$ (Tgfbr2 Control) mice fed a WD (two-tailed Welch's *t*-test). **b**,**d**, Quantification of demyelination (**b**) and IBA1$^{+}$ (**d**) volume at 14dpi in Tgfbr2 control and KO mice treated with tamoxifen 14 days before lesion induction and fed WD (two-tailed Welch's *t*-test). **c**,**f**, Quantification of demyelination (**c**) and IBA1$^{+}$ (**f**) volume at 14dpi in Tgfbr2 control and KO mice treated

with tamoxifen 14 days before lesion induction and fed CD (two-tailed Welch's *t*-test). **e**, Images of corpus callosum lesions at 14 dpi. Scale bar: 200 μm. **g**,**h** Quantification of the number of myelin- (**g**) and crystal-loaded (**h**) $IBA1^+$ cells per $mm^2$ of lesion (two-tailed Welch's *t*-test). **i**, Images of the demyelinated lesion in the corpus callosum at 14dpi showing myelin- and crystal-loaded $IBA1^+$ cells. White arrows point to myelin- and crystal-loaded $IBA1^+$ cells. Scale bar, 20 μm. **j**, The site of action of the conditional genetic knock-out and mode of action of GS in the TGFβ pathway. GS, galunisertib. **k**,**l**, Quantification of demyelination (**k**) and $IBA1^+$ (**l**) volume at 14dpi (one-way Brown-Forsythe and Welch ANOVA tests with multiple comparisons corrected by Dunnett T3 test). **m**, Images of corpus callosum lesions at 14 dpi. Scale bar, 200 μm. **n**,**o**, Quantification of the number of myelin- (**n**) and crystal-loaded (**o**) $IBA1^+$ cells per $mm^2$ of lesion (two-tailed Welch's *t*-test). **p**, Images of the demyelinated lesion in the corpus callosum at 14dpi exemplifying myelin- and crystal-loaded $IBA1^+$ cells. White arrows point to myelin- and crystal-loaded $IBA1^+$ cells. Scale bar, 20μm. *P*-values below 0.1 and *n* numbers are indicated in the figure; each dot represents one mouse. Solid lines in the graphs indicate the mean.

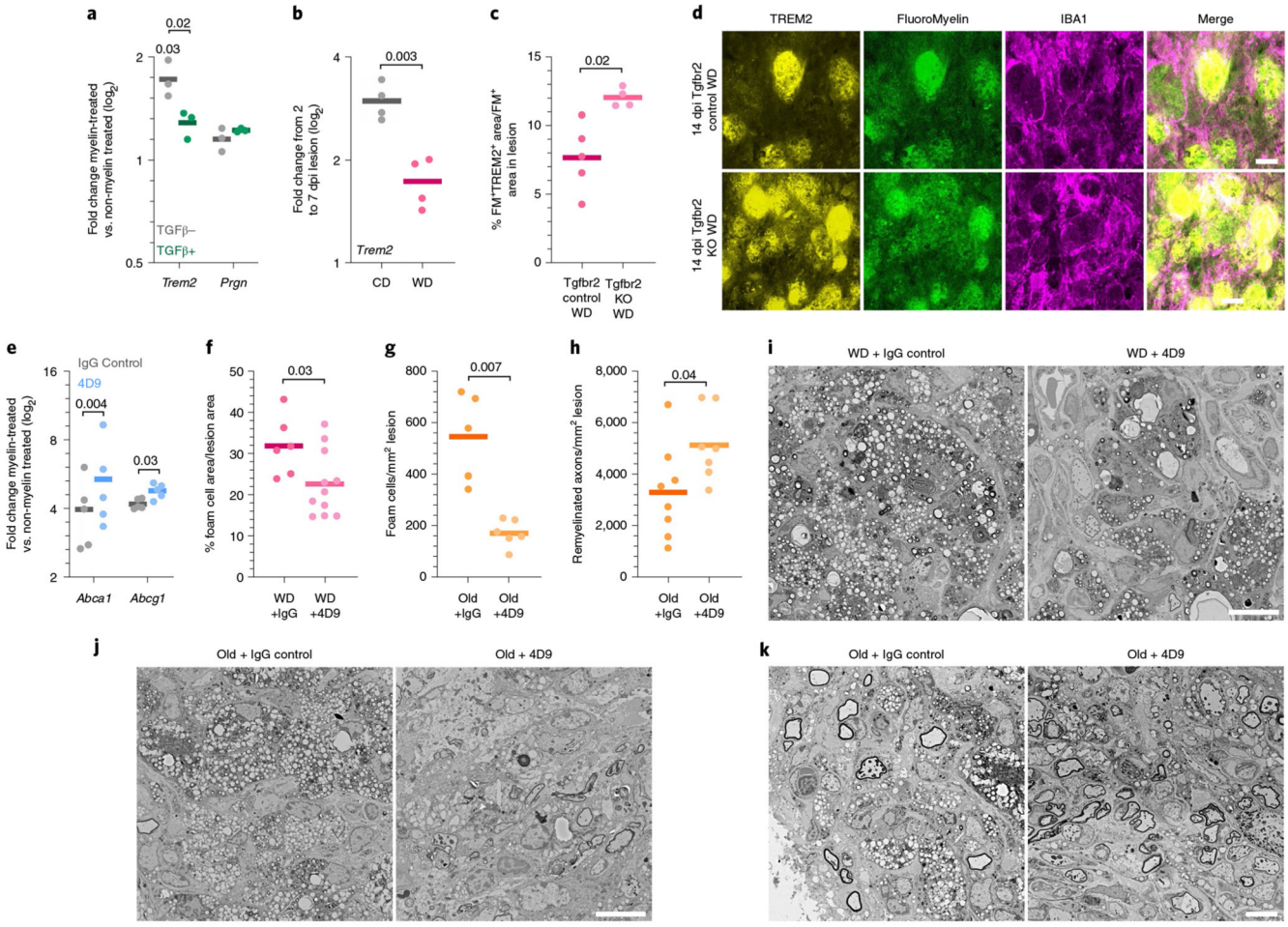


**Fig. 8. Treatment with TREM2-activating monoclonal antibodies 4D9 improves lipid clearance in phagocytes after demyelinating injury.**

**a**, Quantification of the induction of the *Trem2* and *Prgn* expression by myelin intake (*P* for *Trem2* induction = 0.03, one sample *t*-test) and the influence of TGFβ on :his induction (*P* for *Trem2* = 0.02, two-tailed Welch's *t*-test). No significant differences were observed for *Prgn*. **b**, Quantification of the induction of *Trem2* expression in demyelinated lesions from 2 to 7 dpi (two-tailed Welch's *t*-test). **c**, Quantification of TREM2 levels in FluoroMyelin$^{+}$ ($FM^{+}$) cells n the demyelinated lesions at 14dpi (two-tailed Welch's *t*-test). **d**, Images of the demyelinated lesions at 14dpi demonstrating TREM2 expression in myelin-loaded $IBA1^{+}$ cells. Scale bar, 20μm. **e**, Quantification of the expression change in *Abca1* and *Abcg1* upon myelin intake in BMDMs incubated with 4D9 or its isotype control (paired *t*-test). **f**, Quantification of lesion area occupied by foam cells at 14dpi in WD-fed mice treated intraperitoneally with 100 mg/kg (body weight) of 4D9 antibody or its isotype control (two-tailed Welch's *t*-test). **g**, Quantification of the number of foam cells per $mm^2$ of esion at 14 dpi in 12-month-old mice treated intraperitoneally with 100 mg/kg (body weight) 4D9 antibody or its isotype control (two-tailed Welch's :-test). **h**, Quantification of the number of remyelinated axons per $mm^2$ of lesion at 21dpi in 12-month-old mice treated intraperitoneally with 100 mg/kg fbody weight) of 4D9 antibody or its isotype control (two-




Europe PMC Funders Author Manuscripts

tailed Welch's *t*-test). **i**, Electron microscopy images of the demyelinated lesions in the spinal :ord at 14 dpi exemplifying foam-cell accumulation within the lesion. Scale bar, 10 μm. **j**, Electron microscopy images of the demyelinated lesions in the spinal cord at 14dpi exemplifying accumulation of foam cells within the lesion. Scale bar, 10μm. **k**, Electron microscopy images of the demyelinated lesions n the spinal cord at 21 dpi exemplifying remyelinated axons. Scale bar, 10μm. *P*values below 0.1 and *n* numbers are indicated in the figure. Solid lines in he graphs indicate the mean.



Europe PMC Funders Author Manuscripts